J. Fluid Mech. (2011), *vol.* 680, *pp.* 150–193. © Cambridge University Press 2011
doi:10.1017/jfm.2011.154

Steady flow in a rapidly rotating sphere with weak precession

SHIGEO KIDA†

Department of Mechanical Engineering, Doshisha University, Tatara-miyakodani 1-3, Kyotanabe 610-0394, Japan

(Received 1 July 2010; revised 24 January 2011; accepted 26 March 2011; first published online 24 May 2011)

The flow field of an incompressible viscous fluid in a precessing sphere is investigated by the asymptotic analysis for large Reynolds numbers and small Poincaré numbers. The long-standing unsolved equation (Roberts & Stewartson *Astrophys. J.*, vol. 137, 1963, p. 777) for the velocity in the critical region of the boundary layer is solved for the first time in the literature, which enables us to describe explicitly the structure of the conical shear layers spawned from the critical regions into the interior inviscid region. Most of the flux between the boundary layer and the interior is taking place through these conical shear layers. The velocity field in the whole sphere, expanded in a power series of the Poincaré number, is quantitatively determined up to the first order, leaving the solid-body-rotation component to the next-order analysis.

Key words: boundary layer structure, rotating flows

1. Introduction

The flow in a precessing sphere, with spin and precession angular velocities being constant in time, has been extensively studied by many authors since the 1950, as a simple model of the liquid core of the Earth, with primary interest in the generation mechanism of geomagnetism (e.g. Bondi & Lyttleton 1953; Malkus 1968 among others). This system is characterized by three parameters, the Reynolds number Re and the Poincaré number Γ (see (2.4) and (2.5) for definition) as well as the angle between the spin and precession axes. In the above geophysical application, the former two parameters are taken as $Re \gg 1$ and $\Gamma \ll 1$ since they are estimated as $Re \approx 2 \times 10^{13}$ and $\Gamma = 10^{-7}$ for the Earth core (Roberts & Glatzmaier 2000). In this relation we concentrate our attention on the steady (in precession frame) flow for large Reynolds numbers and small Poincaré numbers, i.e. in a rapidly rotating sphere with weak precession.

When the velocity and pressure fields are expanded in a power series of Γ, the leading order $O(\Gamma^0)$ is the solid-body-rotation flow moving together with the sphere itself. The non-trivial flow appears from the first order $O(\Gamma)$. The whole sphere is separated into two regions by the difference in behaviour of the velocity field. One is the boundary layer of thickness $O(Re^{-1/2})$ attached to the sphere surface, in which the tangential (to the surface) component of velocity is $O(\Gamma Re^{1/2})$ and the normal component is $O(\Gamma Re^0)$. The boundary-layer theory, however, breaks down at the critical circles located at polar angles $\pi/3$ and $2\pi/3$ from the spin axis.

† Email address for correspondence: skida@mail.doshisha.ac.jp

https://doi.org/10.1017/jfm.2011.154 Published online by Cambridge University Press

The critical circles are embedded by the critical regions of thickness $O(Re^{-2/5})$ and width $O(Re^{-1/5})$, in which the tangential and normal components of velocity are $O(\Gamma Re^{1/2})$ and $O(\Gamma Re^{3/10})$, respectively. Bondi & Lyttleton (1953) obtained the analytical expression of the velocity profile, which is singular on the critical circles, in the boundary layer. Roberts & Stewartson (1963) discovered the scalings for the size of the critical region and the magnitude of each component of velocity therein. Furthermore, they succeeded in deriving the partial differential equation (equivalent to (4.13*a*) below) for the velocity profile in the critical region. It is curious however that this important equation, which has been referred to repeatedly by many authors since then, has never been solved. The reason of this fact may be attributed to the lack of the boundary conditions to supplement that equation.

The other (complement to the boundary layer) is the interior inviscid region, which occupies the majority of the sphere. The dominant motion here is the solid-body-rotation flow $O(\Gamma R^{1/2})$ whose axis of rotation is perpendicular to the spin axis. The precise analytical expression (equivalent to (4.25*a*) and (4.25*b*)) of the angular velocity and axial direction of this solid-body-rotation flow was obtained by Busse (1968). The velocity field, other than the solid-body-rotation flow, in this region is governed by the linearized Euler equation with Coriolis effects and is explicitly written by the integral forms with an unknown function which must be determined by the normal component of the boundary-layer velocity (Bonti & Lyttleton 1953; see (2.16*a*)–(2.17) below). Again this nice integral formula has never been used practically because the singularity in the normal component of the boundary-layer velocity makes the integrals diverge.

Therefore, unless the singularity at the critical circle were removed, we could not obtain the explicit expression of the velocity distribution (other than the solid-body-rotation flow), even in the leading order, $O(\Gamma)$, which is valid uniformly over the whole sphere. Nevertheless, without that knowledge, the existence and the scaling of the conical shear layers spawned from the critical regions, the most prominent structure in the inviscid region, can be inferred from the hyperbolic nature of the governing equation and the scaling of the flow in the critical region (Greenspan 1968; Kerswell 1995). The thickness of the layer is $O(Re^{1/5})$ and the velocity along the layer is $O(\Gamma Re^{3/10})$. The existence of the conical shear layers has been supported by direct numerical simulations (Hollerbach & Kerswell 1995; Noir, Jault & Cardin 2001*b*; Tilgner & Busse 2001) as well as by experiments (Noir *et al.* 2001*a*).

In this paper the asymptotic analysis in the double limit of $\Gamma \ll 1$ and $Re \gg 1$ is developed to obtain the steady flow of an incompressible viscous fluid in a rapidly rotating sphere with weak precession. The velocity and pressure fields are expanded in a power series of Γ and a set of linear equations for the first-order quantities is derived. According to the standard technique for $Re \gg 1$ we perform the boundary-layer analysis. We re-derive, in a simpler manner, three important results obtained by Bondi & Lyttleton (1953) and Roberts & Stewartson (1963), namely the formal solution for the velocity field in the inviscid region (§ 2), the boundary-layer solution which is singular on critical circles (§ 3) and the partial differential equation for the velocity field in the critical region (§ 4). After deriving necessary boundary conditions, this differential equation is integrated numerically and the velocity field in the critical region is obtained (§ 4). This in turn is used to determine the above formal solution, and then also the velocity field, in the inviscid region (§ 5.1). The velocity field thus obtained is presented in various ways of representation (§§ 5.2 and 5.3). Moreover, the velocity profile in the conical shear layers is derived by the asymptotic analysis applied to the formal solution (§ 5.4).

https://doi.org/10.1017/jfm.2011.154 Published online by Cambridge University Press

2. Formulation

We consider the steady motion of an incompressible viscous fluid in a rapidly rotating sphere with weak precession. The spin and precession angular velocities, denoted respectively by $\boldsymbol{\Omega}_s$ ($\equiv\Omega_s\hat{\boldsymbol{x}}$) and $\boldsymbol{\Omega}_p$ ($\equiv\Omega_p\hat{\boldsymbol{z}}$), are assumed to be constant in magnitude and orthogonal to each other. (Note that a non-orthogonal case of the two rotation axes can be reduced to the orthogonal case as long as the velocity field in the first order in Γ expansion is concerned as in the present paper. See Appendix A.) Here we have introduced the Cartesian (x, y, z) coordinate system that is rotating with precession angular velocity $\boldsymbol{\Omega}_p$. The symbol $\hat{}$ stands for the unit vector.

In a precession frame rotating with $\boldsymbol{\Omega}_p$, the fluid motion is described by the steady Navier–Stokes equation

$$(\boldsymbol{u}\cdot\nabla)\boldsymbol{u}+\nabla p+2\Gamma\hat{\boldsymbol{z}}\times\boldsymbol{u}-\frac{1}{2}\Gamma^2\nabla(\boldsymbol{r}\times\hat{\boldsymbol{z}})^2-\frac{1}{Re}\nabla^2\boldsymbol{u}=0 \tag{2.1}$$

and the continuity equation

$$\nabla\cdot\boldsymbol{u}=0 \tag{2.2}$$

supplemented by the non-slip boundary condition on the sphere surface,

$$\boldsymbol{u}=\hat{\boldsymbol{x}}\times\boldsymbol{r}\quad(\text{on }|\boldsymbol{r}|=1), \tag{2.3}$$

where $\boldsymbol{u}$ is the velocity, p is the pressure, $\boldsymbol{r}$ is the position vector and ∇ is the gradient operator. The third and fourth terms on the left-hand side of (2.1) represent the Coriolis force and the centrifugal force, respectively. All the physical quantities are normalized in terms of the sphere radius a for the length, the reciprocal of the spin angular velocity Ω_s for the time, the kinematic viscosity ν and the density of the fluid. Equation (2.1) has two non-dimensional parameters, namely the Reynolds number

$$Re=\frac{a^2\Omega_s}{\nu} \tag{2.4}$$

and the Poincaré number

$$\Gamma=\frac{\Omega_p}{\Omega_s}. \tag{2.5}$$

In the case of pure rotation ($\Gamma=0$), the system (2.1)–(2.3) yields the solid-body-rotation flow

$$\boldsymbol{u}_{solid}=\hat{\boldsymbol{x}}\times\boldsymbol{r}\ \ (=\hat{\boldsymbol{\varphi}}r\sin\theta), \tag{2.6a}$$

$$p_{solid}=\tfrac{1}{2}|\hat{\boldsymbol{x}}\times\boldsymbol{r}|^2\left(=\tfrac{1}{2}r^2\sin^2\theta\right). \tag{2.6b}$$

Thus, if a weak precession is imposed ($\Gamma\ll1$), we may be able to expand the velocity and pressure fields as a power series of Γ as

$$\boldsymbol{u}=\boldsymbol{u}_{solid}+\Gamma\boldsymbol{u}^{(1)}+\Gamma^2\boldsymbol{u}^{(2)}+\cdots, \tag{2.7a}$$

$$p=p_{solid}+\Gamma p^{(1)}+\Gamma^2 p^{(2)}+\cdots. \tag{2.7b}$$

Substituting (2.7a) and (2.7b) into the system (2.1)–(2.3) and taking the terms $O(\Gamma)$, we obtain

$$(\boldsymbol{u}_{solid}\cdot\nabla)\boldsymbol{u}^{(1)}+(\boldsymbol{u}^{(1)}\cdot\nabla)\boldsymbol{u}_{solid}+\nabla p^{(1)}-\frac{1}{Re}\nabla^2\boldsymbol{u}^{(1)}=-2\hat{\boldsymbol{z}}\times\boldsymbol{u}_{solid}, \tag{2.8}$$

$$\nabla\cdot\boldsymbol{u}^{(1)}=0, \tag{2.9}$$

https://doi.org/10.1017/jfm.2011.154 Published online by Cambridge University Press

and

$$\boldsymbol{u}^{(1)} = 0 \quad (\text{on } |\boldsymbol{r}| = 1). \tag{2.10}$$

Since $\boldsymbol{u}_{solid}$ is symmetric around the x-axis, this linear system admits solutions with a simple symmetry. That is, if we represent the flow field either in the spherical polar coordinate (r, θ, φ) with the x-axis taken as the polar axis or in the cylindrical polar coordinate (x, ρ, φ), the solution may be written as

$$\boldsymbol{u}^{(1)}(r, \theta, \varphi) = \mathrm{Re}(\boldsymbol{v}(r, \theta)\, \mathrm{e}^{\mathrm{i}\varphi}), \quad p^{(1)}(r, \theta, \varphi) = \mathrm{Re}(q(r, \theta)\, \mathrm{e}^{\mathrm{i}\varphi}), \tag{2.11a}$$

or

$$\boldsymbol{u}^{(1)}(x, \rho, \varphi) = \mathrm{Re}(\boldsymbol{v}(x, \rho)\, \mathrm{e}^{\mathrm{i}\varphi}), \quad p^{(1)}(x, \rho, \varphi) = \mathrm{Re}(q(x, \rho)\, \mathrm{e}^{\mathrm{i}\varphi}) \tag{2.11b}$$

in the respective coordinate systems. Here, $\boldsymbol{v}$ and q are complex variables. The system (2.8)–(2.10) admits the velocity field to be anti-symmetric and the pressure field to be symmetric with respect to the origin, that is, $\boldsymbol{u}^{(1)}(\boldsymbol{x}) = -\boldsymbol{u}^{(1)}(-\boldsymbol{x})$ and $p^{(1)}(\boldsymbol{x}) = p^{(1)}(-\boldsymbol{x})$. This symmetry is written in terms of the velocity components and the pressure in the spherical polar coordinate as $v_r(r, \theta) = -v_r(r, \pi - \theta)$, $v_\theta(r, \theta) = +v_\theta(r, \pi - \theta)$, $v_\varphi(r, \theta) = -v_\varphi(r, \pi - \theta)$ and $q(r, \theta) = -q(r, \pi - \theta)$, whereas in the cylindrical polar coordinate as $v_x(x, \rho) = +v_x(-x, \rho)$, $v_\rho(x, \rho) = -v_\rho(-x, \rho)$, $v_\varphi(x, \rho) = -v_\varphi(-x, \rho)$ and $q(x, \rho) = -q(-x, \rho)$.

When the Reynolds number is large ($Re \gg 1$), the thin boundary layer of thickness $O(\delta)$ develops along the sphere surface, where

$$\delta = \frac{1}{\sqrt{Re}} \tag{2.12}$$

is estimated by balancing the advection (first) and the viscous (fourth) terms on the left-hand side of (2.8). Then, the flow structure in the sphere is obtained by examining the equation in the boundary layer and in the inviscid region separately, and matching the solutions in the two regions.

We begin by examining the inviscid region where the viscous term in (2.8) is neglected. Since the flow in the first order of Γ is driven by the Coriolis force due to the solid-body rotation, i.e. the right-hand side of (2.8), it may be natural to assume that the velocity field $\boldsymbol{u}^{(1)}$ is $O(\Gamma)$, the same order in magnitude as this term. However, as will be shown (see (2.18) and below), the velocity of larger order $O(\Gamma\delta^{-1})$ is induced in the inviscid region through the interaction with the boundary-layer flow. Keeping it in mind, we shall start the analysis by assuming that the velocity field is $O(\Gamma)$. The results thus obtained are also applicable for the velocity field $O(\Gamma\delta^{-1})$ only by discarding the source term in (2.8).

In the cylindrical polar coordinate (x, ρ, φ), the Navier–Stokes equation without the viscous term in (2.8) is written as

$$\mathrm{i}v_{Ix} + \frac{\partial q_I}{\partial x} = 2\mathrm{i}\rho, \tag{2.13a}$$

$$-2v_{I\varphi} + \mathrm{i}v_{I\rho} + \frac{\partial q_I}{\partial \rho} = 0, \tag{2.13b}$$

$$2v_{I\rho} + \mathrm{i}v_{I\varphi} + \frac{\mathrm{i}q_I}{\rho} = 0, \tag{2.13c}$$

https://doi.org/10.1017/jfm.2011.154 Published online by Cambridge University Press

where the subscript I stands for the quantities in the inviscid region. The continuity equation (2.9) is written as

$$\frac{\partial v_{Ix}}{\partial x} + \left(\frac{\partial}{\partial \rho} + \frac{1}{\rho}\right) v_{I\rho} + \frac{\mathrm{i}}{\rho} v_{I\varphi} = 0, \tag{2.13d}$$

where $\boldsymbol{v}_I = v_{Ix}\widehat{\boldsymbol{x}} + v_{I\rho}\widehat{\boldsymbol{\rho}} + v_{I\varphi}\widehat{\boldsymbol{\varphi}}$, $\boldsymbol{u}_{solid} = \widehat{\boldsymbol{\varphi}}\rho$ and $\widehat{z} = \widehat{\boldsymbol{\rho}}\sin\varphi + \widehat{\boldsymbol{\varphi}}\cos\varphi$ have been taken into account. The boundary condition on the sphere surface is given by the normal component of velocity, $B(\cos\theta)$ (see (4.21) below), which is specified by the solution at the outer edge of the boundary layer, as

$$v_{Ix}(\cos\theta, \sin\theta)\cos\theta + v_{I\rho}(\cos\theta, \sin\theta)\sin\theta = B(\cos\theta) \quad (\text{for } 0 \leqslant \theta \leqslant \pi). \tag{2.14}$$

After some algebra, (2.13a)–(2.13d) lead to the Poincarè equation

$$\left(\frac{\partial^2}{\partial \rho^2} + \frac{1}{\rho}\frac{\partial}{\partial \rho} - \frac{1}{\rho^2} - 3\frac{\partial^2}{\partial x^2}\right) v_{Ix} = 0. \tag{2.15}$$

The general solution of (2.15) is written as (see Appendix B)

$$v_{Ix}(x, \rho) = \sqrt{3}\int_0^{2\pi} F\left(\frac{1}{2}x + \frac{\sqrt{3}}{2}\rho\cos\lambda\right)\cos\lambda\,\mathrm{d}\lambda, \tag{2.16a}$$

where $F(X)$ ($|X| \leqslant 1$) is a complex function. Then, it is easy to express the other components of velocity and pressure as

$$v_{I\rho}(x, \rho) = 2x - \int_0^{2\pi} F\left(\frac{1}{2}x + \frac{\sqrt{3}}{2}\rho\cos\lambda\right)(1 + \sin^2\lambda)\,\mathrm{d}\lambda, \tag{2.16b}$$

$$v_{I\varphi}(x, \rho) = 2\mathrm{i}x - \mathrm{i}\int_0^{2\pi} F\left(\frac{1}{2}x + \frac{\sqrt{3}}{2}\rho\cos\lambda\right)(1 + \cos^2\lambda)\,\mathrm{d}\lambda, \tag{2.16c}$$

$$q_I(x, \rho) = \mathrm{i}\rho\left[2x - 3\int_0^{2\pi} F\left(\frac{1}{2}x + \frac{\sqrt{3}}{2}\rho\cos\lambda\right)\sin^2\lambda\,\mathrm{d}\lambda\right]. \tag{2.16d}$$

By substituting (2.16a) and (2.16b) into the boundary condition (2.14), we obtain

$$\int_0^{2\pi} F\left(\frac{1}{2}\cos\theta + \frac{\sqrt{3}}{2}\sin\theta\cos\lambda\right)[\sqrt{3}\cos\theta\cos\lambda - \sin\theta(1 + \sin^2\lambda)]\,\mathrm{d}\lambda$$
$$= B(\cos\theta) - 2\sin\theta\cos\theta \quad (\text{for } 0 \leqslant \theta \leqslant \pi). \tag{2.17}$$

Multiplication of $\sin^2\theta\cos\theta$ to (2.17) followed by integration with respect to θ over $[0 : \pi]$ yields

$$\int_0^{\pi} B(\cos\theta)\sin^2\theta\cos\theta\,\mathrm{d}\theta = \frac{8}{15}, \tag{2.18}$$

since the left-hand side of (2.17) is integrated out (see Appendix C). This equation says that the normal component $B(\cos\theta)$ of the velocity $O(\Gamma)$ on the sphere surface is not identically zero so that the tangential components $O(\Gamma\delta^{-1})$ must be excited because the normal component, u_r, in the spherical polar coordinate is smaller by factor $O(\delta)$ than the tangential components, u_θ and u_φ, in the boundary layer. This in turn induces the velocity field $O(\Gamma\delta^{-1})$ in the inviscid region.

The velocity and pressure fields $O(\Gamma\delta^{-1})$, denoted respectively by $\boldsymbol{v}^{[-1]}$ and $q^{[-1]}$, are governed by (2.13a)–(2.14) with the right-hand sides of (2.13a) and (2.14) being

https://doi.org/10.1017/jfm.2011.154 Published online by Cambridge University Press

zero. The solutions are then written as

$$v_{Ix}^{[-1]}(x,\rho)=\sqrt{3}\int_0^{2\pi}F^{[-1]}\left(\frac{1}{2}x+\frac{\sqrt{3}}{2}\rho\cos\lambda\right)\cos\lambda\,\mathrm{d}\lambda, \tag{2.19a}$$

$$v_{I\rho}^{[-1]}(x,\rho)=-\int_0^{2\pi}F^{[-1]}\left(\frac{1}{2}x+\frac{\sqrt{3}}{2}\rho\cos\lambda\right)(1+\sin^2\lambda)\,\mathrm{d}\lambda, \tag{2.19b}$$

$$v_{I\varphi}^{[-1]}(x,\rho)=-\mathrm{i}\int_0^{2\pi}F^{[-1]}\left(\frac{1}{2}x+\frac{\sqrt{3}}{2}\rho\cos\lambda\right)(1+\cos^2\lambda)\,\mathrm{d}\lambda, \tag{2.19c}$$

$$q_I^{[-1]}(x,\rho)=-3\mathrm{i}\rho\int_0^{2\pi}F^{[-1]}\left(\frac{1}{2}x+\frac{\sqrt{3}}{2}\rho\cos\lambda\right)\sin^2\lambda\,\mathrm{d}\lambda, \tag{2.19d}$$

where $F^{[-1]}(X)$ ($|X|\leqslant 1$) is a complex function.

The boundary condition that the radial component of velocity at $O(\Gamma\delta^{-1})$ vanishes on the sphere surface is written as

$$\int_0^{2\pi}F^{[-1]}\left(\frac{1}{2}\cos\theta+\frac{\sqrt{3}}{2}\sin\theta\cos\lambda\right)[\sqrt{3}\cos\theta\cos\lambda-\sin\theta(1+\sin^2\lambda)]\,\mathrm{d}\lambda=0 \quad (\text{for } 0\leqslant\theta\leqslant\pi). \tag{2.20}$$

This equation is satisfied by

$$F^{[-1]}(X)=CX, \tag{2.21}$$

where C is a complex number. It is unknown, however, if this solution is unique or not.

By setting

$$C=\frac{2\mathrm{i}}{3\pi}a\,\mathrm{e}^{\mathrm{i}b}\quad (a \text{ and } b \text{ being real numbers}), \tag{2.22}$$

we find

$$v_{Ix}^{[-1]}(x,\rho)=\mathrm{i}a\,\mathrm{e}^{\mathrm{i}b}\rho, \tag{2.23a}$$

$$v_{I\rho}^{[-1]}(x,\rho)=-\mathrm{i}a\,\mathrm{e}^{\mathrm{i}b}x, \tag{2.23b}$$

$$v_{I\varphi}^{[-1]}(x,\rho)=a\,\mathrm{e}^{\mathrm{i}b}x, \tag{2.23c}$$

$$q_I^{[-1]}(x,\rho)=a\,\mathrm{e}^{\mathrm{i}b}\rho x \tag{2.23d}$$

in the cylindrical polar coordinate or

$$u_{Ix}^{[-1]}(x,\rho,\varphi)=-a\rho\sin(\varphi+b), \tag{2.24a}$$

$$u_{I\rho}^{[-1]}(x,\rho,\varphi)=ax\sin(\varphi+b), \tag{2.24b}$$

$$u_{I\varphi}^{[-1]}(x,\rho,\varphi)=ax\cos(\varphi+b), \tag{2.24c}$$

$$p_I^{[-1]}(x,\rho,\varphi)=a\rho x\cos(\varphi+b) \tag{2.24d}$$

in the spherical polar coordinate. This velocity field represents a solid-body rotation of angular velocity a with the axis being on the (y,z)-plane inclined from the negative y-axis by angle $-b$. That is, the vorticity field is written in the Cartesian coordinate as $\omega_{Ix}^{[-1]}=0$, $\omega_{Iy}^{[-1]}=-2a\cos b$, $\omega_{Iz}^{[-1]}=2a\sin b$.

https://doi.org/10.1017/jfm.2011.154 Published online by Cambridge University Press

To summarize the above analysis in the inviscid region, we have found that

(i) the velocity field is given by a solid-body-rotation flow (the uniqueness of which is open though) at $O(\Gamma\delta^{-1})$ whose magnitude (denoted by a) and direction (denoted by b) are arbitrary;

(ii) the velocity field at $O(\Gamma)$ is represented by integrals as (2.16a)–(2.16c) with a kernel function $F(X)$, which should be determined from the integral equation (2.17) on the sphere surface; and

(iii) the normal component of velocity on the sphere surface at $O(\Gamma)$ must satisfy the integral condition (2.18).

These three facts will be used in the following analysis of the boundary layer as well as the inviscid region in the next order.

3. Boundary layer

In the analysis of the flow in the boundary layer, we adopt the spherical polar coordinate (r, θ, φ) with the x-axis taken as the polar axis and introduce the boundary-layer variables:

$$r = 1 - \delta s, \tag{3.1a}$$
$$v_r(r, \theta) = v_{Bs}(s, \theta), \tag{3.1b}$$
$$v_\theta(r, \theta) = \delta^{-1} v_{B\theta}(s, \theta), \tag{3.1c}$$
$$v_\varphi(r, \theta) = \delta^{-1} v_{B\varphi}(s, \theta), \tag{3.1d}$$
$$q(r, \theta) = \delta^{-1} q_B(s, \theta). \tag{3.1e}$$

In terms of these boundary-layer variables, (2.8) and (2.9) are written as

$$\frac{\partial q_B}{\partial s} = 0, \tag{3.2a}$$
$$\mathrm{i} v_{B\theta} - 2\cos\theta v_{B\varphi} = -\frac{\partial q_B}{\partial \theta} + \frac{\partial^2 v_{B\theta}}{\partial s^2}, \tag{3.2b}$$
$$\mathrm{i} v_{B\varphi} + 2\cos\theta v_{B\theta} = -\frac{\mathrm{i} q_B}{\sin\theta} + \frac{\partial^2 v_{B\varphi}}{\partial s^2}, \tag{3.2c}$$
$$-\frac{\partial v_{Bs}}{\partial s} + \frac{1}{\sin\theta}\frac{\partial}{\partial \theta}(\sin\theta u_{B\theta}) + \frac{\mathrm{i} u_{B\varphi}}{\sin\theta} = 0. \tag{3.2d}$$

The non-slip boundary condition is imposed on the sphere surface:

$$v_{Bs}(0, \theta) = v_{B\theta}(0, \theta) = v_{B\varphi}(0, \theta) = 0. \tag{3.3}$$

On the other hand, the boundary condition at the outer edge ($s \to \infty$) of the boundary layer is given by

$$v_{B\theta}(\infty, \theta) = -\mathrm{i} a\, \mathrm{e}^{\mathrm{i}b}, \tag{3.4a}$$
$$v_{B\varphi}(\infty, \theta) = a\, \mathrm{e}^{\mathrm{i}b} \cos\theta, \tag{3.4b}$$
$$q_B(\infty, \theta) = a\, \mathrm{e}^{\mathrm{i}b} \sin\theta \cos\theta, \tag{3.4c}$$

since the velocity field (2.23a)–(2.23d) in the inviscid region is written, in the spherical polar coordinate, as

$$v_{Ir}^{[-1]}(r, \theta) = 0, \tag{3.5a}$$
$$v_{I\theta}^{[-1]}(r, \theta) = -\mathrm{i} a\, \mathrm{e}^{\mathrm{i}b} r, \tag{3.5b}$$
$$v_{I\varphi}^{[-1]}(r, \theta) = a\, \mathrm{e}^{\mathrm{i}b} r \cos\theta, \tag{3.5c}$$
$$q_I^{[-1]}(r, \theta) = a\, \mathrm{e}^{\mathrm{i}b} r^2 \sin\theta \cos\theta. \tag{3.5d}$$

https://doi.org/10.1017/jfm.2011.154 Published online by Cambridge University Press

It is easy to solve the system (3.2*a*)–(3.4*c*) as (Bondi & Lyttleton 1953; Busse 1968)

$$v_{Bs}(s,\theta) = a\,\mathrm{e}^{\mathrm{i}b}\sqrt{1-\mu^2}\Bigg[-\frac{3(1-\mu)\lambda_-(\mu)}{8\left(\frac{1}{2}-\mu\right)^2}\left(1-\exp[-\lambda_-(\mu)s]\right) + \frac{\mathrm{i}(1+\mu)s}{4\left(\frac{1}{2}-\mu\right)}\exp[-\lambda_-(\mu)s] + \frac{3(1+\mu)\lambda_+(\mu)}{8\left(\frac{1}{2}+\mu\right)^2}\left(1-\exp[-\lambda_+(\mu)s]\right) - \frac{\mathrm{i}(1-\mu)s}{4\left(\frac{1}{2}+\mu\right)}\exp[-\lambda_+(\mu)s]\Bigg], \tag{3.6a}$$

$$v_{B\theta}(s,\theta) = -\frac{\mathrm{i}a\,\mathrm{e}^{\mathrm{i}b}}{2}\left[(1+\mu)\left(1-\exp[-\lambda_-(\mu)s]\right)+(1-\mu)\left(1-\exp[-\lambda_+(\mu)s]\right)\right], \tag{3.6b}$$

$$v_{B\varphi}(s,\theta) = +\frac{a\,\mathrm{e}^{\mathrm{i}b}}{2}\left[(1+\mu)\left(1-\exp[-\lambda_-(\mu)s]\right)-(1-\mu)\left(1-\exp[-\lambda_+(\mu)s]\right)\right], \tag{3.6c}$$

$$q_B(s,\theta) = a\,\mathrm{e}^{\mathrm{i}b}\sin\theta\cos\theta, \tag{3.6d}$$

where

$$\lambda_\pm^2 = \mathrm{i}(1\pm 2\mu) \quad (\mathrm{Re}(\lambda_\pm)\geqslant 0), \tag{3.7a}$$

or

$$\lambda_\pm(\mu) = \left(1+\mathrm{sgn}\left(\tfrac{1}{2}\pm\mu\right)\mathrm{i}\right)\left|\tfrac{1}{2}\pm\mu\right|^{\frac{1}{2}}, \tag{3.7b}$$

and sgn stands for the sign function.

We note that the functions $\lambda_\pm(\mu)$ are singular (non-differentiable) at $\mu=\mp 1/2$. As a result, the tangential components $v_{B\theta}(s,\theta)$ and $v_{B\varphi}(s,\varphi)$ of velocity are non-differentiable with respect to μ at $\mu=\mp 1/2$. Moreover, the factors $(1/2\pm\mu)$ in the denominator of the individual terms in (3.6*a*) make the radial component $v_{Bs}(s,\theta)$ diverge at these positions. These are known as the critical circles (Bondi & Lyttleton 1953). Mathematically these are the positions where the left-hand sides of (3.2*b*) and (3.2*c*) degenerate: they are identical for $\cos\theta=\pm 1/2$. Physically this singularity is caused by a resonance of the Coriolis and rotation effects of the solid-body-rotation flow $\boldsymbol{u}_{solid}$ on the first-order velocity field $\boldsymbol{u}^{(1)}$. The Coriolis force (the right-hand side of (2.8)) reads $-2\sin\theta\sin\varphi$ in the boundary layer, which introduces $\boldsymbol{u}^{(1)}$, the sinusoidal modulation of the fundamental mode in φ. The advection terms (the first two on the left-hand side of (2.8)) including $\boldsymbol{u}_{solid}$, on the other hand, rotate the tangential velocity (u_θ, u_φ) with angular velocity $2\cos\theta$ along φ to induce the sinusoidal modulation of frequency $2\cos\theta$ in φ. These two effects resonate at $2\cos\theta=\pm 1$.

In figure 1 we show the boundary-layer solution $u_{Br}=\mathrm{Re}[v_{Bs}\,\mathrm{e}^{\mathrm{i}\varphi}]$, $u_{B\theta}=\delta^{-1}\mathrm{Re}[v_{B\theta}\,\mathrm{e}^{\mathrm{i}\varphi}]$, $u_{B\varphi}=\delta^{-1}\mathrm{Re}[v_{B\varphi}\,\mathrm{e}^{\mathrm{i}\varphi}]$ in the Mercator projection on the angular (φ,θ) surfaces for six radial positions. The velocity components on the angular surfaces are shown by projected streamlines with arrows, whereas the radial component by contours with positive regions being shadowed. At the outer edge of the boundary layer (figure 1*f*), the tangential components $(u_{B\theta}, u_{B\varphi})$ show the solid-body rotation with the axis pointed to $(\mu,\varphi)=(0,-b+\pi)$ to connect with the inviscid flow (2.24*a*)–(2.24*c*). This swirling motion is observed throughout the boundary layer. Nearer the sphere surface ($(f)\to(a)$) it is deformed more from the solid-body rotation, and the swirling centre shifts towards decreasing φ and comes to $\varphi=-b+3\pi/4$ on the boundary (figure 1*a*). The velocity field varies rapidly near the critical circles $\mu=\pm 1/2$. The tangential components jump in direction across them, whereas the radial component u_{Bs} diverges on them.

https://doi.org/10.1017/jfm.2011.154 Published online by Cambridge University Press

https://doi.org/10.1017/jfm.2011.154 Published online by Cambridge University Press

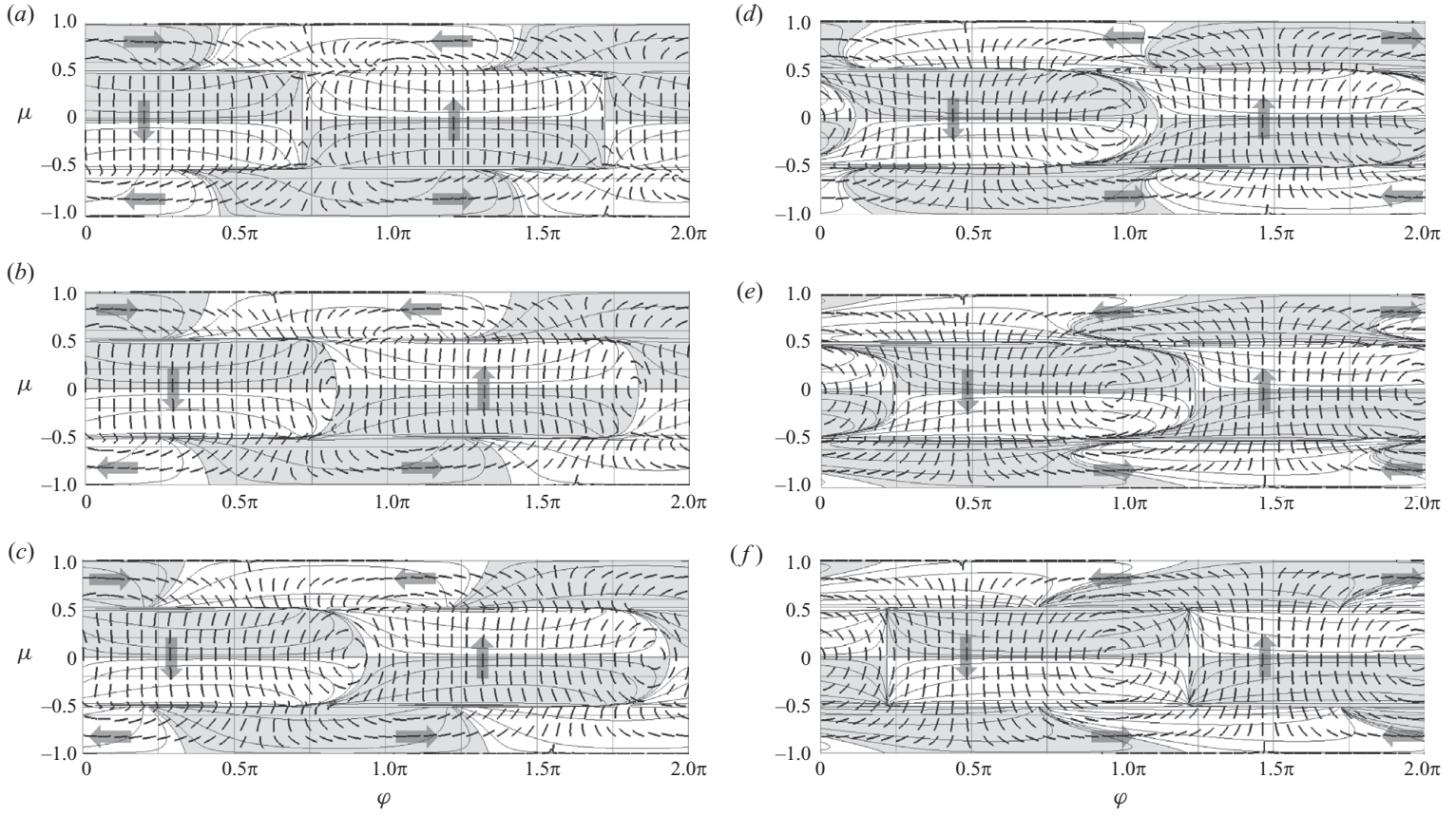


FIGURE 1. The boundary-layer solution of the velocity field in the Mercator projection on the (φ, μ)-planes for six radial positions: (*a*) $s \to 0$, (*b*) 1, (*c*) 2, (*d*) 4, (*e*) 8, (*f*) ∞. The in-plane components $(u_{B\varphi}, u_{B\theta})$ of velocity are shown by projected streamlines with arrows indicating the flow direction, whereas the radial component u_{Bs} by contour lines with levels of $\pm 2 \times 4^{(n-3)}$ $(n = 0, 1, 2, \ldots)$ with positive parts being shadowed. Observe that $(u_{B\varphi}, u_{B\theta})$ jumps in direction at $\mu = \pm 1/2$, whereas u_{Bs} diverges there.

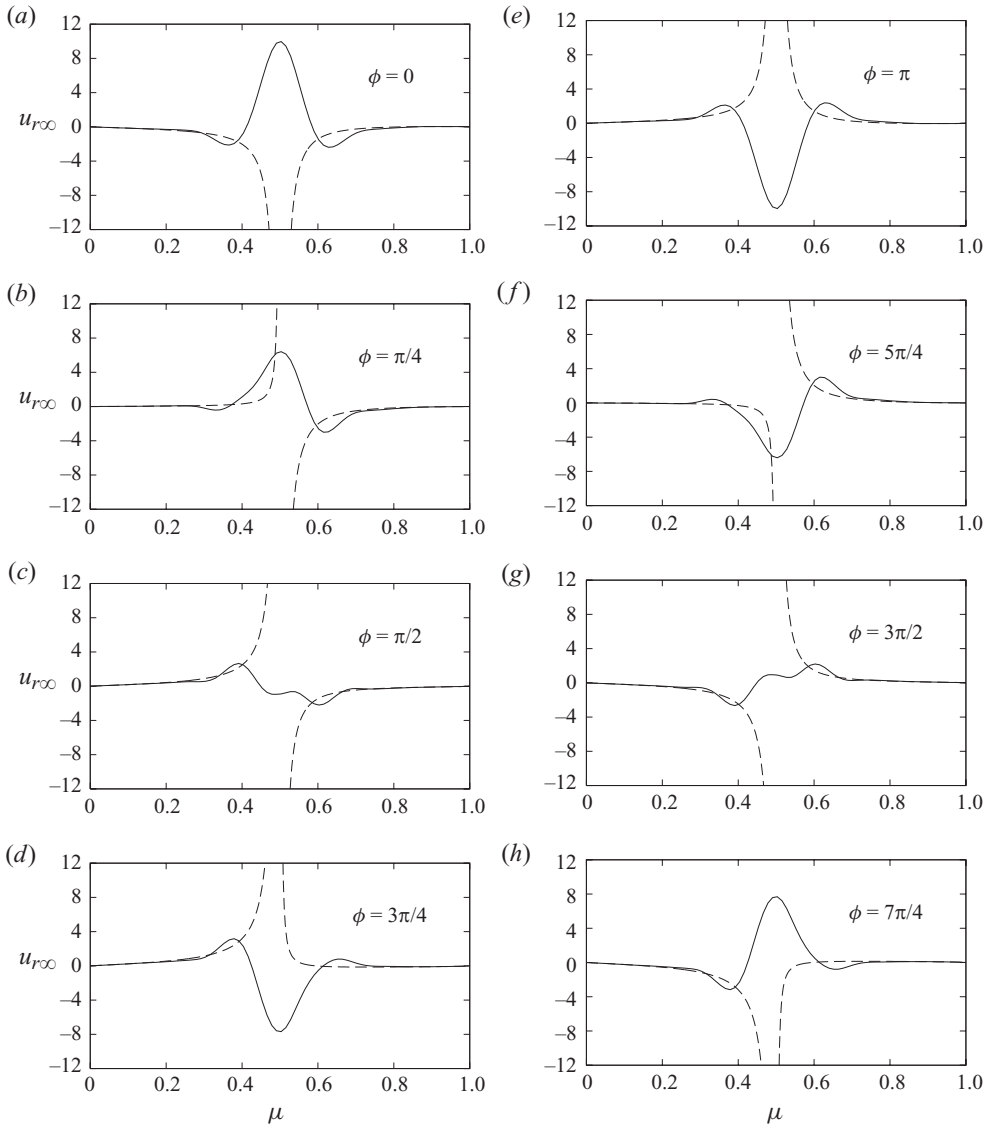


FIGURE 2. Radial component of velocity $u_{r\infty}(\mu, \varphi)$ at the outer edge of the boundary layer. The boundary-layer solution with and without correction in the critical region (for $\delta = 10^{-3}$) are shown with solid and dashed lines, respectively. (*a*) $\varphi = 0$, (*b*) $\pi/4$, (*c*) $\pi/2$, (*d*) $3\pi/4$, (*e*) π, (*f*) $5\pi/4$, (*g*) $3\pi/2$, (*h*) $7\pi/4$.

At the outer edge of the boundary layer, the radial component of velocity (3.6*a*) is written as

$$v_{Bs}(\infty, \theta) = \frac{3a\,\mathrm{e}^{\mathrm{i}b}\sqrt{1-\mu^2}}{8}\left[\frac{(1+\mu)\lambda_+(\mu)}{\left(\frac{1}{2}+\mu\right)^2} - \frac{(1-\mu)\lambda_-(\mu)}{\left(\frac{1}{2}-\mu\right)^2}\right], \tag{3.8}$$

since the exponential terms are negligibly small. In figure 2 we plot, with dashed lines, $u_{r\infty}(\mu, \varphi) = \mathrm{Re}(v_{Bs}(\infty, \theta)\,\mathrm{e}^{\mathrm{i}\varphi})$ for positive $\mu = \cos\theta$ and eight values of φ between 0 and π (n.b. the symmetry $u_{r\infty}(\mu, \varphi) = -u_{r\infty}(-\mu, \varphi) = -u_{r\infty}(\mu, \varphi + \pi)$). Here, the constants a and b are taken from (4.25*a*, 4.25*b*) below. Since singular at $\mu = \pm 1/2$,

https://doi.org/10.1017/jfm.2011.154 Published online by Cambridge University Press

this solution is useless for the boundary condition of the velocity in the inviscid region because not only the integral (2.18) but also the right-hand side of (2.17) diverge. This divergence problem will be solved in the next section. Then, it will be justified that the integral (2.18) may be used to determine a and b by taking the principal value (see (4.22)).

4. Critical region

The boundary-layer solution diverges on the critical circles, $\mu = \pm 1/2$. An asymptotic analysis around this circle was performed, in a similar problem – the motion of a rotating fluid with a free surface – by Roberts & Stewartson (1963) who found new scaling laws, as (4.12), and derived a partial differential equation, as (4.13a), to describe the velocity field there. However, this equation has never been solved in the literature probably because of the lack of associated boundary conditions. Here we solve this problem.

Recall that the terms including $\lambda_-(\mu)$ in the velocity (3.6a)–(3.6c) are singular at $\mu = 1/2$, whereas the ones including $\lambda_+(\mu)$ at $\mu = -1/2$ and that the pressure field (3.6d) is regular throughout the boundary layer. Here we analyse the flow in the vicinity of $\mu = 1/2$ since the flow is symmetric with respect to the equator.

We pick up the singular parts of the velocity and pressure fields as

$$v^S_{Bs}(s,\theta) = a\,\mathrm{e}^{\mathrm{i}b}\sqrt{1-\mu^2}\left[-\frac{3(1-\mu)\lambda_-(\mu)}{8\left(\frac{1}{2}-\mu\right)^2}\left(1-\exp[-\lambda_-(\mu)s]\right) + \frac{\mathrm{i}(1+\mu)s}{4\left(\frac{1}{2}-\mu\right)}\exp[-\lambda_-(\mu)s]\right], \tag{4.1a}$$

$$v^S_{B\theta}(s,\theta) = \frac{\mathrm{i}a\,\mathrm{e}^{\mathrm{i}b}}{2}(1+\mu)\exp[-\lambda_-(\mu)s], \tag{4.1b}$$

$$v^S_{B\varphi}(s,\theta) = -\frac{a\,\mathrm{e}^{\mathrm{i}b}}{2}(1+\mu)\exp[-\lambda_-(\mu)s], \tag{4.1c}$$

$$q^S_B(s,\theta) = 0, \tag{4.1d}$$

which will be replaced by the critical-region solution below.

Since the boundary-layer scaling (3.1a)–(3.1e) fails at the critical circles, we must find another appropriate scaling. Let us introduce the scaling exponents α and β in the radial and latitudinal directions respectively as

$$r = 1 - \delta^\alpha \xi, \tag{4.2a}$$

$$\mu = \tfrac{1}{2} + \delta^\beta \eta. \tag{4.2b}$$

We assume that

$$\alpha > \beta > 0. \tag{4.3}$$

In the vicinity of $\mu = 1/2$, the singular parts of the velocity field (4.1a)–(4.1c) are expanded in power series of δ^β as

$$v^S_{Bs}(\xi,\eta) = -\frac{\sqrt{3}a\,\mathrm{e}^{\mathrm{i}b}}{2\delta^{\frac{3}{2}\beta}}\left[\frac{3[1-\mathrm{sgn}(\eta)\mathrm{i}]}{16|\eta|^{\frac{3}{2}}}\left(1-\exp[-\delta^{\alpha+\frac{1}{2}\beta-1}[1-\mathrm{sgn}(\eta)\mathrm{i}]|\eta|^{\frac{1}{2}}\xi]\right) + \frac{3\mathrm{i}\xi}{8\eta}\exp\left[-\delta^{\alpha+\frac{1}{2}\beta-1}[1-\mathrm{sgn}(\eta)\mathrm{i}]|\eta|^{\frac{1}{2}}\xi\right] + \cdots\right], \tag{4.4a}$$

https://doi.org/10.1017/jfm.2011.154 Published online by Cambridge University Press

$$v^S_{B\theta}(\xi,\eta)=\frac{3\mathrm{i}a\,\mathrm{e}^{\mathrm{i}b}}{4}\exp\left[-\delta^{\alpha+\frac{1}{2}\beta-1}[1-\mathrm{sgn}(\eta)\mathrm{i}]|\eta|^{\frac{1}{2}}\xi\right]\left[1+\frac{2}{3}\delta^{\beta}\eta+\cdots\right], \quad (4.4b)$$

$$v^S_{B\varphi}(\xi,\eta)=-\frac{3a\,\mathrm{e}^{\mathrm{i}b}}{4}\exp\left[-\delta^{\alpha+\frac{1}{2}\beta-1}[1-\mathrm{sgn}(\eta)\mathrm{i}]|\eta|^{\frac{1}{2}}\xi\right]\left[1+\frac{2}{3}\delta^{\beta}\eta+\cdots\right], \quad (4.4c)$$

where use has been made of $s=\delta^{\alpha-1}\xi$ and $\lambda_-(\mu)=\delta^{\beta/2}[1-\mathrm{sgn}(\eta)\mathrm{i}]|\eta|^{1/2}$. We demand

$$\alpha+\tfrac{1}{2}\beta=1 \quad (4.5)$$

so that the singular parts are well behaved as functions of ξ and η. Inequality (4.3) and equation (4.5) lead to inequality $0<\beta<2/3$ which implies that $|v^S_{Bs}|\ll|v^S_{B\theta}|, |v^S_{B\varphi}|$.

The order of magnitude of velocity near the critical circle may be estimated from (3.1*a*)–(3.1*e*) and (4.4*a*)–(4.4*c*) as $v_r(r,\theta)=O(\delta^{-3\beta/2})$, $v_\theta(r,\theta)=O(\delta^{-1})$ and $v_\varphi(r,\theta)=O(\delta^{-1})$. Then we expand the solution in power series of δ^β as

$$v_r(r,\theta)=\delta^{-\frac{3}{2}\beta}\left(v_{C\xi}(\xi,\eta)+\delta^{\beta}v^{(1)}_{C\xi}(\xi,\eta)+\cdots\right), \quad (4.6a)$$

$$v_\theta(r,\theta)=\delta^{-1}\left(v_{C\eta}(\xi,\eta)+\delta^{\beta}v^{(1)}_{C\eta}(\xi,\eta)+\cdots\right), \quad (4.6b)$$

$$v_\varphi(r,\theta)=\delta^{-1}\left(v_{C\varphi}(\xi,\eta)+\delta^{\beta}v^{(1)}_{C\varphi}(\xi,\eta)+\cdots\right). \quad (4.6c)$$

In this scaling the term containing $v_{C\varphi}$ in the continuity equation is negligible, and we obtain

$$\frac{\partial v_{C\xi}}{\partial\xi}+\frac{\sqrt{3}}{2}\frac{\partial v_{C\eta}}{\partial\eta}=0. \quad (4.7)$$

The leading order in the Navier–Stokes equation for the radial component of velocity gives

$$-\sqrt{3}v_{C\varphi}=\frac{\partial q_C}{\partial\xi} \quad (4.8a)$$

with the scaling

$$q(r,\theta)=\delta^{-\frac{1}{2}\beta}\left(q_C(\xi,\eta)+\delta^{\beta}q^{(1)}_C(\xi,\eta)+\cdots\right), \quad (4.8b)$$

where (4.5) has been taken into account.

Substituting the expansions (4.6*a*)–(4.6*c*) and (4.8*b*) into the Navier–Stokes equations, we obtain, up to the next order in δ expansion,

$$\mathrm{i}v_{C\eta}-v_{C\varphi}+\left(-2\delta^{\beta}\eta v_{C\varphi}-\frac{\sqrt{3}}{2}\delta^{1-\frac{3}{2}\beta}\frac{\partial p_C}{\partial\eta}-\delta^{\beta}\frac{\partial^2 v_{C\eta}}{\partial\xi^2}+\mathrm{i}\delta^{\beta}v^{(1)}_{C\eta}-\delta^{\beta}v^{(1)}_{C\varphi}\right)+\cdots=0, \quad (4.9a)$$

$$\mathrm{i}v_{C\varphi}+v_{C\eta}+\left(2\delta^{\beta}\eta v_{C\eta}+\sqrt{3}\delta^{1-\frac{3}{2}\beta}v_{C\xi}-\delta^{\beta}\frac{\partial^2 v_{C\varphi}}{\partial\xi^2}+\mathrm{i}\delta^{\beta}v^{(1)}_{C\varphi}+\delta^{\beta}v^{(1)}_{C\eta}\right)+\cdots=0 \quad (4.9b)$$

for the θ- and φ-components, respectively. Here, use has been made of (4.3) and $\cos\theta=1/2+\delta^{\beta}\eta+\cdots$.

The leading orders, $O(1)$, i.e. the first two terms, in (4.9*a*) and (4.9*b*) give the same equation

$$v_{C\varphi}=\mathrm{i}v_{C\eta}. \quad (4.10)$$

Since they are degenerate, we must examine the next order to determine the solution.

https://doi.org/10.1017/jfm.2011.154 Published online by Cambridge University Press

Those terms included in brackets in (4.9a) and (4.9b) constitute the next order. The most general solution is obtained when all of these terms are of the same order, i.e.

$$-2\eta v_{C\varphi} - \frac{\sqrt{3}}{2}\frac{\partial q_C}{\partial \eta} - \frac{\partial^2 v_{C\eta}}{\partial \xi^2} + \mathrm{i}v^{(1)}_{C\eta} - v^{(1)}_{C\varphi} = 0, \tag{4.11a}$$

$$2\eta v_{C\eta} + \sqrt{3}v_{C\xi} - \frac{\partial^2 v_{C\varphi}}{\partial \xi^2} + \mathrm{i}v^{(1)}_{C\varphi} + v^{(1)}_{C\eta} = 0 \tag{4.11b}$$

with $\beta = 1 - 3\beta/2$, which leads together with (4.5) to (Roberts & Stewartson 1963)

$$\alpha = \tfrac{4}{5}, \quad \beta = \tfrac{2}{5}. \tag{4.12}$$

A combination of (4.7), (4.8a), (4.10), (4.11a) and (4.11b) gives

$$\left[\frac{\partial^3}{\partial \xi^3} + \mathrm{i}\left(2\eta\frac{\partial}{\partial \xi} - \frac{3}{2}\frac{\partial}{\partial \eta}\right)\right]\frac{\partial Q}{\partial \xi} = 0 \quad (|\eta| > 0,\ \xi > 0), \tag{4.13a}$$

where $Q(\xi, \eta)$ has been introduced through

$$q_C(\xi, \eta) = \frac{3\sqrt{3}a\,\mathrm{e}^{\mathrm{i}b}}{4} Q(\xi, \eta). \tag{4.13b}$$

It should be noted here that the highest derivative terms with respect to η have been neglected in the Navier–Stokes equation in the derivation of (4.13a), implying that the solution to (4.13a) may be continuous but not be differentiable at $\eta = 0$. Once Q (therefore q_C) is obtained, $v_{C\varphi}$ is calculated from (4.8a), then $v_{C\eta}$ from (4.10) and then $v_{C\xi}$ from (4.7) as

$$v_{C\xi} = -\frac{3\sqrt{3}\mathrm{i}}{8} a\,\mathrm{e}^{\mathrm{i}b}\frac{\partial Q}{\partial \eta}, \tag{4.14a}$$

$$v_{C\eta} = \frac{3\mathrm{i}}{4} a\,\mathrm{e}^{\mathrm{i}b}\frac{\partial Q}{\partial \xi}, \tag{4.14b}$$

$$v_{C\varphi} = -\frac{3}{4} a\,\mathrm{e}^{\mathrm{i}b}\frac{\partial Q}{\partial \xi}. \tag{4.14c}$$

Recall that the singular parts of the boundary-layer solution are expressed in terms of the critical-region variables ξ and η as (4.4a)–(4.4c). By comparing them with (4.6a)–(4.6c) and putting $\xi = 0$, we obtain $v_{C\xi}(0, \eta) = 0$, $v_{C\eta}(0, \eta) = 3\mathrm{i}a\,\mathrm{e}^{\mathrm{i}b}/4$, $v^{(1)}_{C\eta}(0, \eta) = \mathrm{i}a\,\mathrm{e}^{\mathrm{i}b}\eta/2$, $v_{C\varphi}(0, \eta) = -3a\,\mathrm{e}^{\mathrm{i}b}/4$ and $v^{(1)}_{C\varphi}(0, \eta) = -a\,\mathrm{e}^{\mathrm{i}b}\eta/2$. These conditions, together with (4.8a) and (4.9b) at $\xi = 0$, give

$$\frac{\partial Q}{\partial \xi}(0, \eta) = 1 \quad (|\eta| > 0), \tag{4.15a}$$

$$\frac{\partial^3 Q}{\partial \xi^3}(0, \eta) = -2\mathrm{i}\eta \quad (|\eta| > 0). \tag{4.15b}$$

Since the singular part of the pressure field in the boundary layer is null (see (4.1d)), we have

$$Q(0, \eta) = 0 \quad (|\eta| > 0). \tag{4.15c}$$

As seen in (4.4c), the azimuthal components of velocity tend to zero as $\xi \to \infty$. Thus we have

$$\frac{\partial Q}{\partial \xi}(\xi, \eta) \to 0 \quad (|\eta| > 0,\ \xi \to \infty). \tag{4.15d}$$

https://doi.org/10.1017/jfm.2011.154 Published online by Cambridge University Press

The system (4.13*a*)–(4.15*d*) admits the Hermite symmetry with respect to η to the solution:

$$Q(\xi, \eta) = Q^*(\xi, -\eta), \tag{4.16}$$

where * stands for the complex conjugate, which is consistent with the symmetry of the singular parts of the boundary-layer solution (4.4*a*)–(4.4*c*) without the factor $a\,\mathrm{e}^{\mathrm{i}b}$ around the critical circle. We assume this symmetry. Then we have, at $\eta = 0$, that

$$\mathrm{Im}\ Q(\xi, 0) = 0 \quad (\xi > 0). \tag{4.17a}$$

The imaginary part of (4.13*a*) yields $\mathrm{Re}(\partial^2 Q/\partial\xi\,\partial\eta) = 0$, the integration of which with respect to ξ leads to

$$\mathrm{Re}\left(\frac{\partial Q}{\partial \eta}(\xi, 0)\right) = 0 \quad (\xi > 0), \tag{4.17b}$$

where the boundary condition (4.15*c*) has been taken into account.

Incidentally, by taking the limit $\xi \to 0$ and $|\eta| \to \infty$ with $|\eta|^{1/2}\xi$ being finite of the singular parts of the boundary-layer velocity (4.4*a*)–(4.4*c*) and comparing with (4.14*a*)–(4.14*c*), we obtain

$$Q(\xi, \eta) \to \frac{\mathrm{sgn}(\eta)\mathrm{i}(1 - \mathrm{sgn}(\eta)\mathrm{i})}{2|\eta|^{1/2}}\left(1 - \exp\left[-(1 - \mathrm{sgn}(\eta)\mathrm{i})|\eta|^{\frac{1}{2}}\xi\right]\right)$$
$$\text{as } \xi \to 0,\ |\eta| \to \infty\ \left(|\eta|^{\frac{1}{2}}\xi \text{ being finite}\right). \tag{4.18}$$

This condition is not imposed on the differential equation (4.13*a*) because it is of first order in the η derivative. It turns out, however, that the resulting solution will satisfy this condition (see figures 4 and 5). The asymptotic behaviour (4.18) suggests that the pressure may take large values in the critical region, as it actually does (see (5.38*d*)).

We solve (4.13*a*) numerically by the finite difference scheme under the boundary conditions (4.15*a*)–(4.15*d*), (4.17*a*) and (4.17*b*). Although the fourth-order differential (with respect to ξ) equation (4.13*a*) can be integrated once leading to a third-order one, we do not do it because the numerical solution to the third-order one did diverge. The fourth-order central difference scheme is employed for the first-, second- and fourth-order derivatives in (4.13*a*) (the second-order scheme led to a divergence of numerical solution). For the first-order differential with respect to η, on the other hand, we adopt the first-order backward difference scheme because the second-order central difference scheme led to an oscillatory divergence. As for the boundary condition, the fourth-order central difference scheme is adopted for (4.15*a*), and the fourth-order forward scheme for (4.15*b*).

The computational domain is taken as a rectangle $0 \leqslant \xi \leqslant L_\xi$, $0 \leqslant \eta \leqslant L_\eta$ with N_ξ and M_η mesh points in ξ and η, respectively. We checked the accuracy by changing the computational domain as well as the number of mesh points. In figure 3 we plot the contours of $Q(\xi, \eta)$ calculated for $(L_\xi, L_\eta) = (8, 10)$ and $(N_\xi, M_\eta) = (81, 101)$. The real and imaginary parts are symmetric and anti-symmetric with respect to η, respectively. The contour lines are nearly vertical at larger ξ (> 6, say), suggesting that the computational domain may be sufficient enough for the function to approach an asymptotic limit. This limit is shown in figure 4, where the cross-sections of (*a*) the real and (*b*) the imaginary parts of $Q(\xi, \eta)$ on line $\xi = 8$ are drawn with solid curves together with the corresponding asymptote (4.18) of the boundary-layer solution with dashed curves. We see how the singularity of the boundary-layer solution is resolved by the critical-region solution at $\eta = 0$. The two solutions are nearly identical for $|\eta| > 3$. The vertical cross-sections of $Q(\xi, \eta)$ are shown on lines $\eta = 2$, 5 and 10 in

https://doi.org/10.1017/jfm.2011.154 Published online by Cambridge University Press

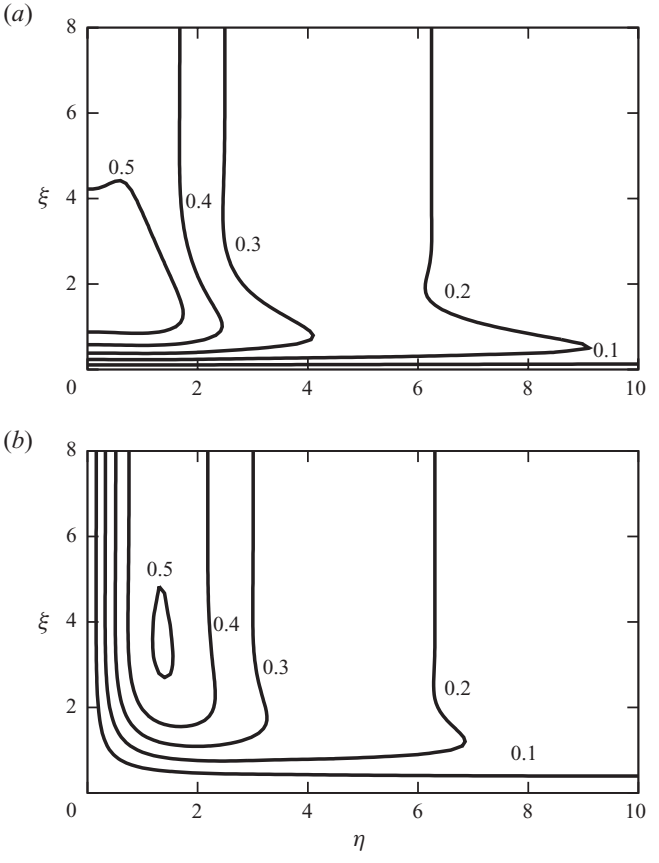


FIGURE 3. Contours of the critical-region solution $Q(\xi, \eta)$. (*a*) Real part. (*b*) Imaginary part. The levels of contour lines are indicated by the attached numbers. The real and imaginary parts are symmetric and anti-symmetric with respect to η, respectively.

figure 5. The agreement between the two solutions is excellent for $\eta = 5$ and 10 but not for $\eta = 2$. This is consistent with the above observation. As recognized from the crossing of the lines around $|\eta| = 2$ in figure 4(*a*), good agreement of the two lines of $\mathrm{Re}(Q)$ for $\eta = 2$ is accidental.

Since the function $Q(\xi, \eta)$ expresses the singular part of the pressure field as

$$p_C(\xi, \eta, \varphi) = \mathrm{Re}\left(\frac{3\sqrt{3}}{4} a Q \exp[\mathrm{i}(\varphi + b)]\right) = \frac{3\sqrt{3}a}{4}\left[\mathrm{Re}(Q)\cos(\varphi + b) - \mathrm{Im}(Q)\sin(\varphi + b)\right], \quad (4.19)$$

$\mathrm{Re}(Q)$ (figures 3*a*–5*a*) represent the pressure distribution at $\varphi = -b$, whereas $\mathrm{Im}(Q)$ (figures 3*b*–5*b*) that at $3\pi/2 - b$. They have a peak at a finite location $\xi \leqslant 4$ and $|\eta| \leqslant 2$, showing that the pressure in the critical region is quite large.

Once the function $Q(\xi, \eta)$ was known, the three components of velocity in the critical region can be calculated by (4.14*a*)–(4.14*c*). For example, the radial component

https://doi.org/10.1017/jfm.2011.154 Published online by Cambridge University Press

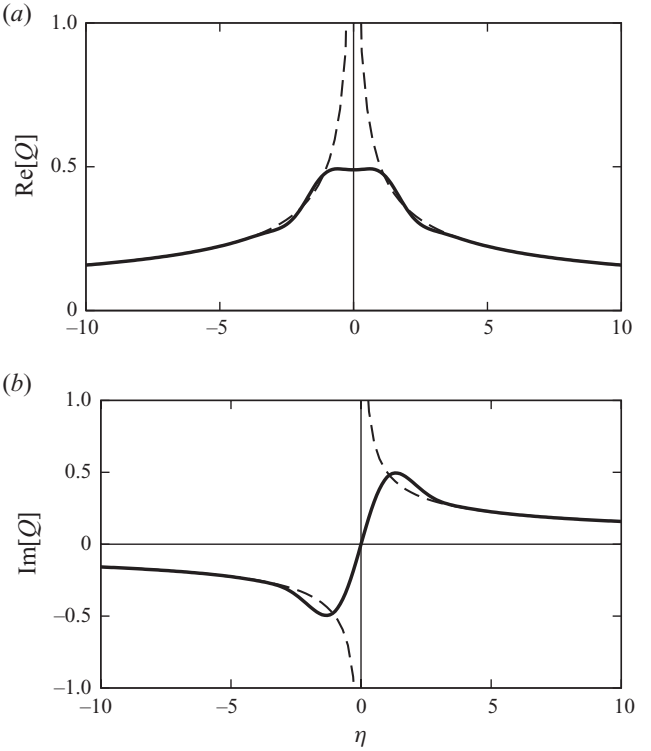


FIGURE 4. Cross-sections of the critical-region solution $Q(\xi, \eta)$ on line $\xi = 8$. (*a*) Real part. (*b*) Imaginary part. The dashed lines indicate the asymptote (4.18).

is written as

$$u_\xi(\xi, \eta, \varphi) = \mathrm{Re}\left(-\mathrm{iexp}[\mathrm{i}(\varphi + b)]\frac{\partial Q}{\partial \eta}\right)$$
$$= \mathrm{Re}\left(\frac{\partial Q}{\partial \eta}\right)\sin(\varphi + b) + \mathrm{Im}\left(\frac{\partial Q}{\partial \eta}\right)\cos(\varphi + b). \quad (4.20)$$

In figure 6 we plot $\partial Q/\partial \eta$ versus η for $\xi = 1$, 2, 4 and 8. The left column shows the real part which represents the radial component of velocity at $\varphi = \pi/2 - b$, whereas the right column the imaginary part which represents that at $\varphi = -b$. We note that the bottom panels ($\xi = 8$) on the right and left columns roughly correspond to figures 2(*a*) and 2(*c*), respectively, because $|b| \ll 1$ (see (4.25*b*)). Now it is clear how the singularity of the boundary-layer solution is regularized in the critical region. It is a bit surprising and impressive that the real parts of the two solutions behave in an exactly opposite way around $\eta = 0$. In other words, a simple extrapolation of the boundary-layer solution there could not predict the behaviour of the critical-region solution. As a matter of fact, the integral of the imaginary part of the critical-region solution over the whole domain vanishes. The real part is also integrated out because it is odd with respect to η. This fact is closely related to the success of the principal value integral (4.22) discussed below.

The radial component of velocity at the outer edge of the boundary layer is written, after correcting the boundary-layer solution (3.8) by the critical-region solution around

https://doi.org/10.1017/jfm.2011.154 Published online by Cambridge University Press

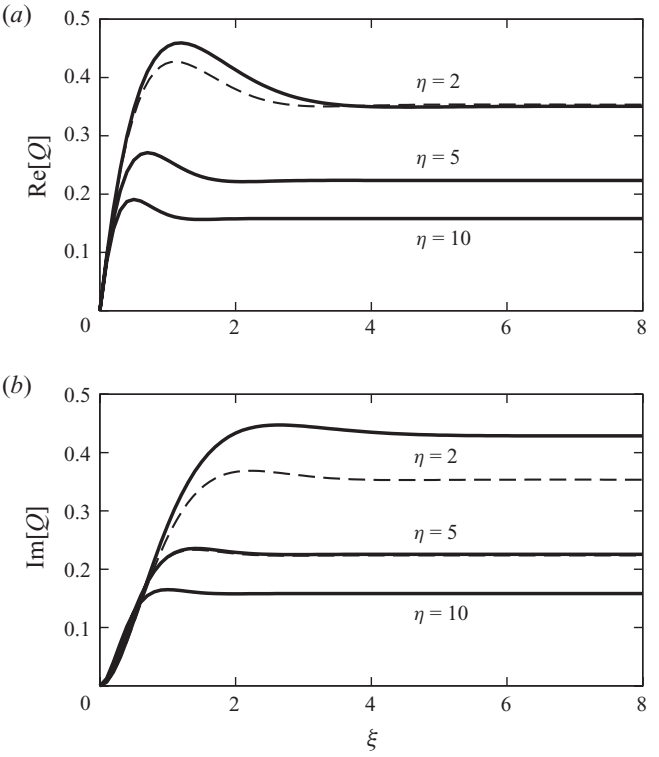


FIGURE 5. Same as figure 4 but on lines $\eta = 2$, 5 and 10.

$\mu = \pm 1/2$, as

$$B(\mu) = \begin{cases} -\dfrac{3\sqrt{3}\mathrm{i}a\,\mathrm{e}^{\mathrm{i}b}}{8}\left\{\delta^{-\frac{3}{5}}\dfrac{\partial Q_\infty^*}{\partial\eta}(\eta_-) - \dfrac{\mathrm{i}\sqrt{1-\mu^2}(1-\mu)\lambda_-(\mu)}{\sqrt{3}\left(\frac{1}{2}-\mu\right)^2}\right\} & \left(|\mu+\tfrac{1}{2}| < \mu_c\right), \\ -\dfrac{3\sqrt{3}\mathrm{i}a\,\mathrm{e}^{\mathrm{i}b}}{8}\left\{\dfrac{\mathrm{i}\sqrt{1-\mu^2}(1+\mu)\lambda_+(\mu)}{\sqrt{3}\left(\frac{1}{2}+\mu\right)^2} + \delta^{-\frac{3}{5}}\dfrac{\partial Q_\infty}{\partial\eta}(\eta_+)\right\} & \left(|\mu-\tfrac{1}{2}| < \mu_c\right), \\ -\dfrac{3\sqrt{3}\mathrm{i}a\,\mathrm{e}^{\mathrm{i}b}}{8}\left(\dfrac{\mathrm{i}\sqrt{1-\mu^2}}{\sqrt{3}}\right)\left[\dfrac{(1+\mu)\lambda_+(\mu)}{\left(\frac{1}{2}+\mu\right)^2} - \dfrac{(1-\mu)\lambda_-(\mu)}{\left(\frac{1}{2}-\mu\right)^2}\right] & \text{(otherwise)}, \end{cases} \tag{4.21}$$

where $Q_\infty(\eta) = Q(\infty, \eta)$, $\eta_\pm = \delta^{-2/5}(\mu \mp 1/2)$ and $O(\delta^{2/5}) \ll O(\mu_c) \ll O(1)$. This function has the properties that $B(\mu) = -B(-\mu)$ and $B(1) = B(-1) = 0$.

For this corrected boundary-layer solution at the outer edge, the integral in (2.18) does converge not only for finite δ but also in the limit $\delta \to 0$. This convergence may be a little surprising and would not be easily anticipated from the singular behaviour of the boundary-layer solution (shown by dashed lines in figure 2). Once the critical-region solution is known, however, the convergence of the integral in (2.18) is quite reasonable and the proof is straightforward (not shown here).

Now we calculate the integral in the limit $\delta \to 0$. We change the integral variable from θ to $\mu = \cos\theta$ and substitute the solution (4.21) for $B(\mu)$ and take the limit

https://doi.org/10.1017/jfm.2011.154 Published online by Cambridge University Press

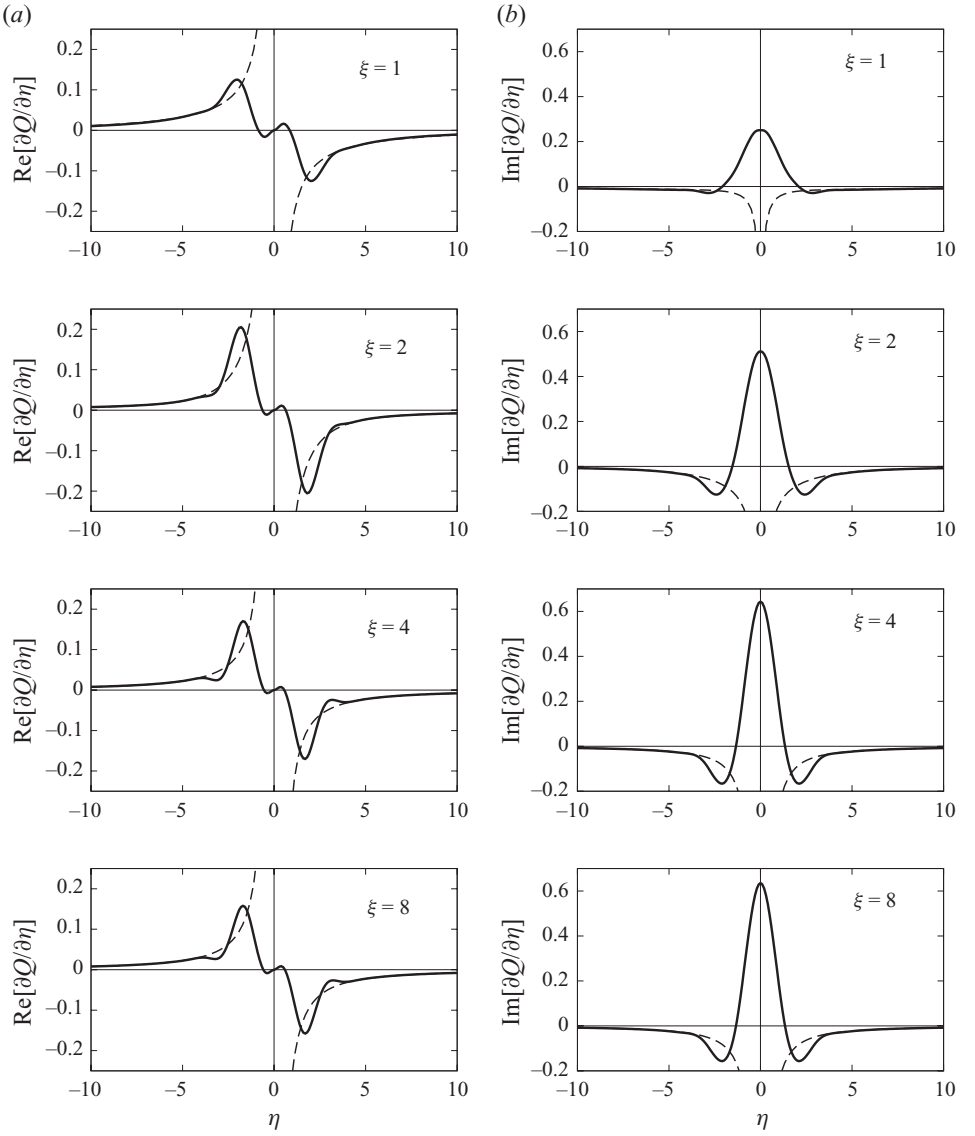


FIGURE 6. The η derivative of the critical-region solution $\partial Q/\partial\eta$. The real and imaginary parts are shown in the left and right columns, respectively. The thick solid line represents the critical-region solution, whereas the dashed line indicates the asymptote (4.18) of the boundary-layer solution.

$\delta \to 0$ to obtain

$$\frac{8}{15} = \frac{3a\,\mathrm{e}^{\mathrm{i}b}}{4}\ \mathrm{P.V.}\int_{-1}^{1} \frac{\mu(1+\mu)(1-\mu^2)\left(1+\mathrm{sgn}\left(\frac{1}{2}+\mu\right)\mathrm{i}\right)}{\left|\frac{1}{2}+\mu\right|^{\frac{3}{2}}}\,\mathrm{d}\mu, \tag{4.22}$$

where P.V. implies the principal value integral (at $\mu = -1/2$). We have used the fact that the function $B(\mu)$ is composed of two terms anti-symmetric with respect to μ with each other. We deform the integral path from a segment $[-1 : 1]$ on the real

https://doi.org/10.1017/jfm.2011.154 Published online by Cambridge University Press

axis to a line in the lower complex μ-plane ($\mathrm{Im}(\mu)<0$) and rewrite the integral as

$$\frac{8}{15}=\frac{3a\,\mathrm{e}^{\mathrm{i}b}}{4}\sqrt{2}\,\mathrm{e}^{\frac{\pi}{4}\mathrm{i}}\int_{-1}^{1}\mu(1+\mu)(1-\mu^2)\left(\tfrac{1}{2}+\mu\right)^{-3/2}\mathrm{d}\mu. \\ (\mathrm{Im}(\mu)<0). \tag{4.23}$$

By changing further the integration variable from μ to ζ through $2\mu+1=3\zeta^2$, this equation is written as

$$\frac{8}{15}=\frac{3\sqrt{3}a\,\mathrm{e}^{\mathrm{i}b}}{16}\,\mathrm{e}^{\frac{\pi}{4}\mathrm{i}}\int_{-\frac{\mathrm{i}}{\sqrt{3}}}^{1}\frac{(1-\zeta^2)(3\zeta^2+1)^2(3\zeta^2-1)}{\zeta^2}\,\mathrm{d}\zeta \\ =\frac{\sqrt{2}a\,\mathrm{e}^{\mathrm{i}b}}{35}\left[(19+9\sqrt{3})-(19-9\sqrt{3})\mathrm{i}\right]. \tag{4.24}$$

This leads to

$$a=\frac{14\sqrt{151}}{453}=0.3797\cdots, \tag{4.25a}$$

$$b=\arctan\left(\frac{19-9\sqrt{3}}{19+9\sqrt{3}}\right)=0.09831\cdots(\mathrm{rad})=5.63\cdots(\mathrm{deg}). \tag{4.25b}$$

Then, the solid-body-rotation flow in the inviscid region is determined as

$$\boldsymbol{u}_I=\left[\widehat{\boldsymbol{x}}-\frac{7\sqrt{2}(19+9\sqrt{3})}{906}\Gamma\delta^{-1}\widehat{\boldsymbol{y}}+\frac{7\sqrt{2}(19-9\sqrt{3})}{906}\Gamma\delta^{-1}\widehat{\boldsymbol{z}}\right]\times\boldsymbol{r}+O(\Gamma). \tag{4.26}$$

This result completely agrees with the one derived by Busse (1968) (see his expression (3.19) and (A 2*a*) in Appendix A).

5. Inviscid region

Now that the radial component of velocity at the outer edge of the boundary layer was obtained as (4.21), we can solve the boundary condition (2.17) for the interior flow. Before going into the analysis, a comment on the validity of the inviscid analysis may be in order because the appearance of strong thin shear layers, originated from the critical-region solution in (4.21), makes it non-trivial. It turns out that the thickness and strength of the shear layers are $O(\delta^{2/5})$ and $O(\Gamma\delta^{-3/5})$ (see (5.38*a*)–(5.38*c*)), respectively. Therefore the viscous term is smaller than the other terms by a factor $\delta^{3/5}$ $(=\delta^2\times\delta^{-3/5}\times\delta^{2\times(-2/5)})$, which may justify the inviscid analysis of the interior flow at $O(\Gamma)$ by the use of (4.21).

5.1. *Solution to (2.17)*

We solve (2.17) with a given $B(\mu)$ by the Legendre-polynomial expansion (see appendix D). We multiply (2.17) by $\sin^2\theta P_{2n+1}(\cos\theta)$ and integrate it with respect to θ over the interval $[0,\pi]$, where $P_{2n+1}(\cos\theta)$ is the Legendre polynomial of the $(2n+1)$st order, n being an integer. By expanding the unknown function $F(\cos\theta)$ in an infinite series of Legendre polynomials as

$$F(\cos\theta)=\sum_{n=0}^{\infty}F_n P_{2n+1}(\cos\theta), \tag{5.1}$$

https://doi.org/10.1017/jfm.2011.154 Published online by Cambridge University Press

we obtain an infinite set of linear simultaneous equations for the coefficients F_n $(n = 1, 2, \ldots)$,

$$M_{1,1}F_1 + M_{1,2}F_2 = B_1 + \frac{8}{35}, \tag{5.2a}$$

$$M_{n,n-1}F_{n-1} + M_{n,n}F_n + M_{n,n+1}F_{n+1} = B_n \quad (n = 2, 3, \ldots), \tag{5.2b}$$

where

$$B_n = \int_0^\pi B(\cos\theta)\sin^2\theta P_{2n+1}(\cos\theta)\,\mathrm{d}\theta \quad (n = 1, 2, \ldots) \tag{5.3}$$

and

$$M_{n,n-1} = \frac{2\pi}{(4n-1)(4n+1)(4n+3)}\left[6n(2n+1)P_{2n+1}\left(\frac{1}{2}\right) + 4\sqrt{3}nP^1_{2n+1}\left(\frac{1}{2}\right) + P^2_{2n+1}\left(\frac{1}{2}\right)\right], \tag{5.4a}$$

$$M_{n,n} = \frac{2\pi}{4n+3}\left\{\left[\frac{3}{4n+3}\left(\frac{(2n+1)^2}{4n+1} + \frac{(2n+2)^2}{4n+5}\right) - 3\right]P_{2n+1}\left(\frac{1}{2}\right) - \frac{2\sqrt{3}}{2n+2}\left[\frac{1}{4n+3}\left(\frac{(2n+1)^2}{4n+1} + \frac{(2n+2)^2}{4n+5}\right) - \frac{2n+1}{4n+1}\right]P^1_{2n+1}\left(\frac{1}{2}\right) + \frac{1}{(2n+2)(2n+3)}\left[\frac{1}{4n+3}\left(\frac{(2n+1)^2}{4n+1} + \frac{(2n+2)^2}{4n+5}\right) - \frac{4n+3}{4n+1}\right]P^2_{2n+1}\left(\frac{1}{2}\right)\right\}, \tag{5.4b}$$

$$M_{n,n+1} = \frac{2(2n+2)(2n+3)\pi}{(4n+3)(4n+5)(4n+7)}\left[3P_{2n+1}\left(\frac{1}{2}\right) - \frac{2\sqrt{3}}{2n+2}P^1_{2n+1}\left(\frac{1}{2}\right) + \frac{1}{(2n+2)(2n+3)}P^2_{2n+1}\left(\frac{1}{2}\right)\right], \tag{5.4c}$$

where P^1_{2n+1} and P^2_{2n+1} are the associated Legendre polynomials of the first and second degrees. Note that $M_{1,0} = 0$ and that the coefficient F_0 is not included in the above set of equations. This coefficient is determined in the next order in the δ expansion (not performed here).

For a given δ ($\ll 1$), the simultaneous equations (5.2*a*) and (5.2*b*) are solved numerically by the following six steps.

(i) The function $Q(\xi, \eta)$ is obtained by solving the partial differential equation (4.13*a*) under the boundary conditions (4.15*a*)–(4.15*d*), (4.17*a*) and (4.17*b*).

(ii) The radial component $B(\mu)$ of velocity at the outer edge is calculated by the use of (4.21).

(iii) The coefficients B_n on the right-hand sides of (5.2*a*) and (5.2*b*) are obtained by numerical integration of (5.3).

(iv) The coefficients F_n are calculated by solving the simultaneous equations (5.2*a*) and (5.2*b*) truncated at a given order N. We set $N = 400$, 400 and 2000 for $\delta = 10^{-4}$, 10^{-5} and 10^{-6}, respectively.

(v) The function $F(\mu)$ is obtained from a finite series of (5.1) (see Appendix D for the appropriate collocation points).

(vi) The velocity and pressure fields are calculated by (2.16*a*)–(2.16*d*) and (2.11*b*).

https://doi.org/10.1017/jfm.2011.154 Published online by Cambridge University Press

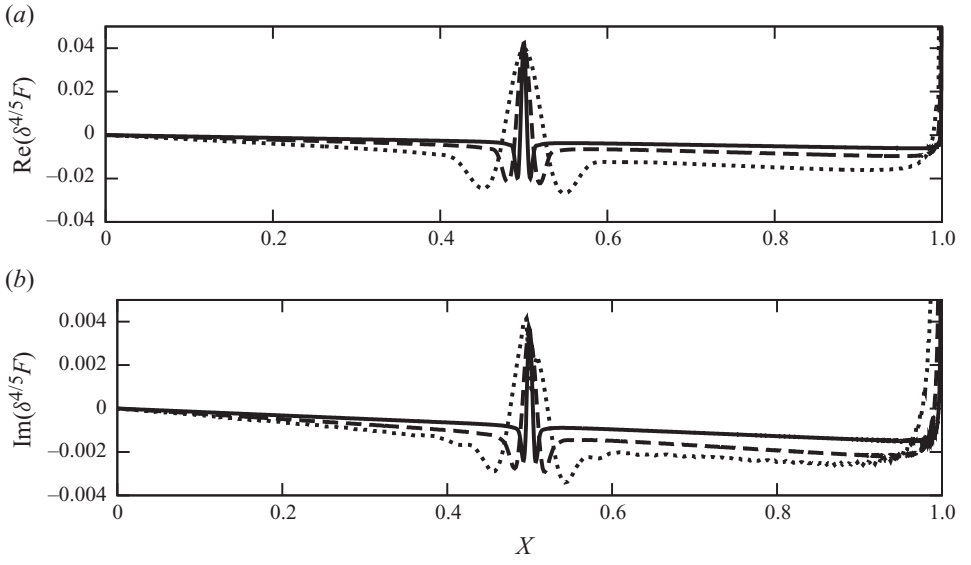


FIGURE 7. Function $F(X)$. The real and imaginary parts are drawn in (a) and (b), respectively. The dotted, dashed and solid lines indicate the cases of $\delta = 10^{-4}$, 10^{-5} and 10^{-6}, respectively. The vertical axis is scaled by $\delta^{4/5}$ so that the peak value around $X = 1/2$ may be comparable between the three cases. There are two sharp peaks around $X = 1/2$ and 1, which are enlarged in figure 15.

In figure 7 we plot the function $F(X)$ obtained at step (v) for $\delta = 10^{-4}$ (dotted lines), 10^{-5} (dashed lines) and 10^{-6} (solid lines). Only the region of positive X is shown because $F(X)$ is odd. The real part is drawn in (a) and the imaginary part in (b). The function is multiplied by $\delta^{4/5}$ so that the peak value around $X = 1/2$ may be comparable between the three cases (see (5.16b)). It is seen that the function $F(X)$ takes extremely large values in the neighbourhoods of $X = 1/2$ and 1. The peaks are higher and narrower for smaller values of δ. As will be shown later in § 5.4, the appearance of these two sharp peaks is closely related to the critical region in the boundary layer, and the one around $X = 1/2$ is essential to the formation of thin conical shear layers.

5.2. *Conical shear layer*

We calculate the velocity and pressure fields in the inviscid region by the use of numerical data of F (step (vi) listed in § 5.1). The x-, ρ- and φ-components of velocity and the pressure are respectively written, from (2.16a)–(2.16d), as

$$u_x(x, \rho, \varphi) = \sqrt{3} \int_0^{2\pi} (F_r(X)\cos\varphi - F_i(X)\sin\varphi)\cos\lambda \, \mathrm{d}\lambda, \tag{5.5a}$$

$$u_\rho(x, \rho, \varphi) = 2x\cos\varphi + \frac{1}{2}\int_0^{2\pi} (F_r(X)\cos\varphi - F_i(X)\sin\varphi)(-3 + \cos 2\lambda)\, \mathrm{d}\lambda, \tag{5.5b}$$

$$u_\varphi(x, \rho, \varphi) = -2x\sin\varphi + \frac{1}{2}\int_0^{2\pi} (F_r(X)\sin\varphi + F_i(X)\cos\varphi)(3 + \cos 2\lambda)\, \mathrm{d}\lambda, \tag{5.5c}$$

$$p(x, \rho, \varphi) = -2x\rho\sin\varphi + \frac{3}{2}\rho\int_0^{2\pi} (F_r(X)\sin\varphi + F_i(X)\cos\varphi)(1 - \cos 2\lambda)\, \mathrm{d}\lambda \tag{5.5d}$$

https://doi.org/10.1017/jfm.2011.154 Published online by Cambridge University Press

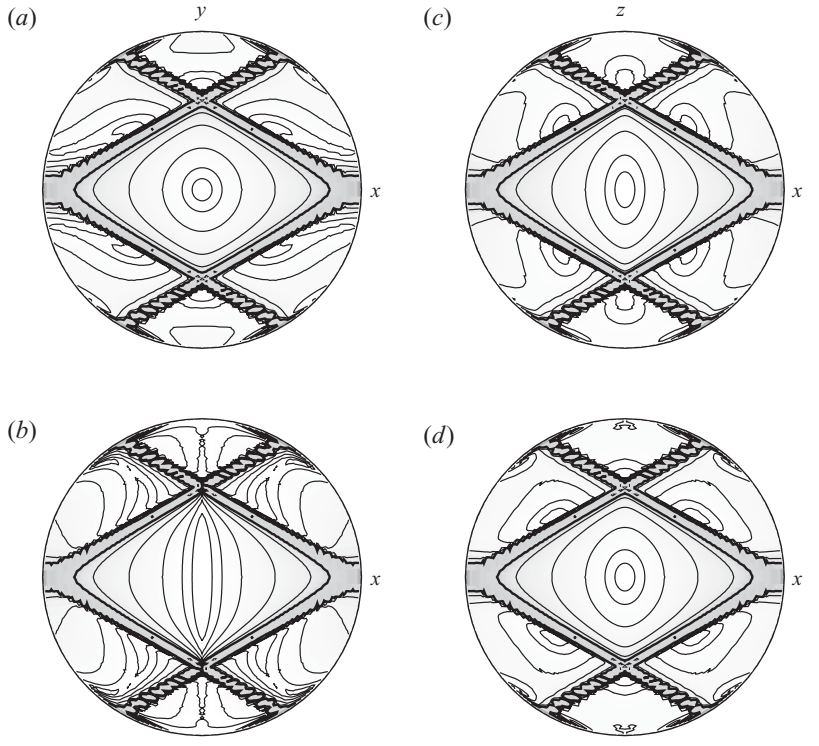


FIGURE 8. The velocity magnitude on the meridional planes. The levels of contours are 1.25×2^n, $(n = 0, 1, 2, 3, 4, 5)$, being higher in darker regions. (*a*) $\varphi/\pi = 0$, (*b*) 1/4, (*c*) 1/2, (*d*) 3/4. $\delta = 10^{-6}$.

where

$$X = \frac{1}{2}x + \frac{\sqrt{3}}{2}\rho\cos\lambda, \tag{5.6}$$

and the subscripts r and i of $F(X)$ stand for the real and imaginary parts, respectively.

The integration with respect to λ is performed by the use of trapezoidal rule with 10 000 mesh points. In figure 8 we plot the contours of velocity magnitude on four meridional planes, $\varphi/\pi = 0$, 1/4, 1/2 and 3/4, for $\delta = 10^{-6}$. The contour levels are 1.25×2^n $(n = 0, \ldots, 5)$ with higher values being indicated by darker grey. We see that the areas of largest velocity, the darker areas sandwiched by thick curves (contours of 1.25×2^5), are identical in all the four cross-sections, implying that the velocity field is axi-symmetric around the x-axis. There are two strong conical shear layers connecting the critical circles at polar angles $\pi/3$ and $2\pi/3$ from the x-axis and the poles located at two far side ends of the x-axis. We denote the cones with apex at $(x, y, z) = (\pm 1, 0, 0)$ by $\mathscr{C}_\pm$, respectively (see (5.37)). The thickness of the shear layer is $O(\delta^{2/5}) \sim 0.004$ (see below).

As will be shown in § 5.4 (see (5.38*c*) and (5.44*a*, 5.44*b*)), the thickness of the conical shear layers is $O(\delta^{2/5})$, and the velocity across the layers is $O(\Gamma\delta^{-3/5})$ and dominated by the tangential component, whose magnitude changes as $1/\sqrt{q_\pm}$, where $q_\pm$ is the distance from the apex of $\mathscr{C}_\pm$, and whose angle (to the generating line) varies as $\varphi + b$. The velocity field has such a symmetry with respect to the (y, z)-plane that $u_x \to +u_x$, $u_y \to -u_y$, $u_z \to -u_z$ as $x \to -x$. Therefore, the velocity profile across the conical shear layers may be easily imagined from a couple of their cross-sections.

https://doi.org/10.1017/jfm.2011.154 Published online by Cambridge University Press

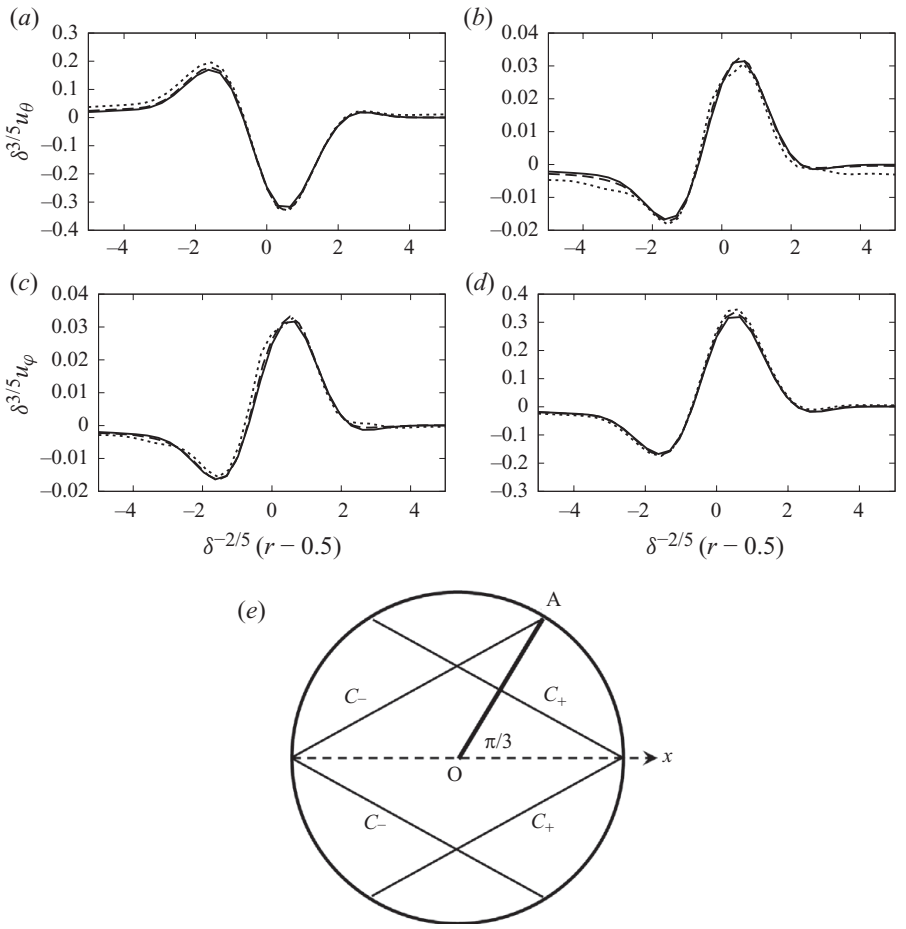


FIGURE 9. The velocity profile across the shear layer at $\theta = \pi/3$. (*a*) u_θ at $\varphi = 0$, (*b*) u_θ at $\varphi = \pi/2$, (*c*) u_φ at $\varphi = 0$, (*d*) u_φ at $\varphi = \pi/2$, (*e*) line OA is orthogonal to cone $\mathscr{C}_+$. The radial coordinate of the cross-point is $r = 0.5$. The dotted, dashed and solid lines indicate the cases of $\delta = 10^{-4}$, 10^{-5} and 10^{-6}, respectively.

In figure 9 we show the velocity profile (in *a–d*) across the shear layer along a radial line (OA in *e*) and perpendicular to the cone $\mathscr{C}_+$. The θ-components (which are parallel to the conical surface at the cross point $r = 1/2$) of velocity at $\varphi = 0$ and $\pi/2$ are respectively drawn in (*a*) and (*b*), whereas the φ-components in (*c*) and (*d*). The dotted, dashed and solid lines indicate the cases of $\delta = 10^{-4}$, 10^{-5} and 10^{-6}, respectively. The abscissa and the ordinate are normalized by the width $O(\delta^{2/5})$ and the velocity $O(\Gamma\delta^{-3/5})$ of the shear layer. The overlapping of the three types of lines implies that this scaling law is well satisfied. It is impressive that the curves of (*b*) and (*c*) are nearly identical, and those of (*a*) and (*d*) are nearly mirror-symmetric with respect to the horizontal axis. This is a manifestation of the sinusoidal dependence of the velocity components on φ (see (5.45*a*, 5.45*b*)). We see that the variation of velocity is large around $r = 1/2$ where the shear layer is located and that there are two peaks of opposite senses. The magnitude of the peaks is larger for the far side from the sphere centre.

This velocity distribution is consistent with one of the results obtained numerically by Noir, *et al.* (2001*b*) both in shape and magnitude. See their figure 3(*a*), where the

https://doi.org/10.1017/jfm.2011.154 Published online by Cambridge University Press

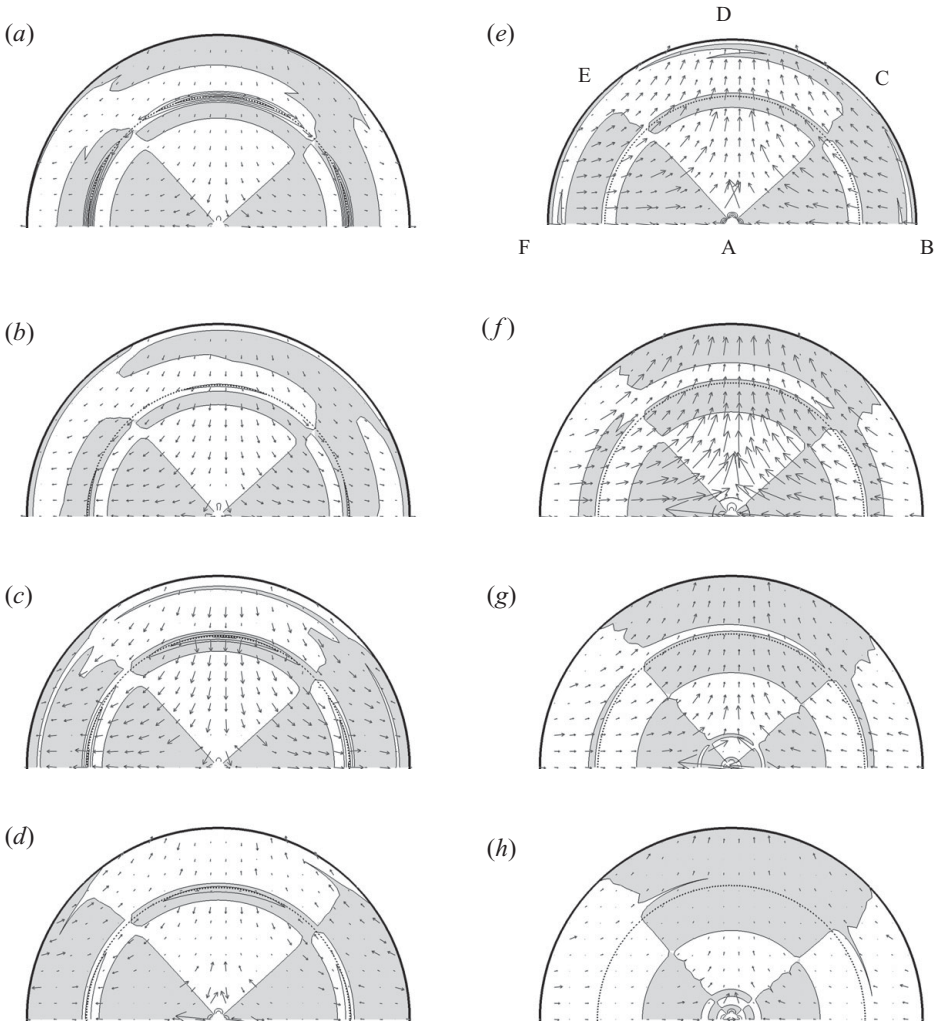


FIGURE 10. The flow in the conical shear layer belonging to $\mathscr{C}_+$. The velocity field is drawn on eight conical slices of the layer separated outwards by (*a*) $p_+ = -0.016$, (*b*) -0.012, (*c*) -0.008, (*d*) -0.004, (*e*) 0, (*f*) 0.004, (*g*) 0.008, (*h*) 0.012, where p_+ is the distance between the individual slices and $\mathscr{C}_+$. The in-plane component is represented by arrows and the normal component by grey for direction of inside-out and white for outside-in. Point A in (*e*) indicates the apex of $\mathscr{C}_+$, and lines AB, AC, AD, AE and AF the cross-lines of the planes of azimuthal angles $\varphi = 0$, $\pi/2$, π, $3\pi/2$ and 2π with the cone, respectively. The velocity field in the vicinity of A is discarded for brevity. $\delta = 10^{-6}$.

θ-component of velocity is plotted. (Note that the unit of their velocity is different from ours. They take it from the magnitude of the solid-body -rotation flow $O(\Gamma\delta^{-1})$ so that their velocity scales as $\Gamma\delta^{-3/5}$ $(= \delta^{2/5} \times \Gamma\delta^{-1})$ which is exactly same as ours.) The φ-component of velocity (their figure 3*b*) has more oscillations (about the double) along the radius than the θ-component. This disagrees with the present theory (described in § 5.4), in which the two components have the same structure (see (5.45*a*, 5.45*b*)).

The velocity distribution in the shear layer may be best seen by slicing the layer. In figure 10 we plot the velocity field for $\delta = 10^{-6}$ in the shear layer belonging to

https://doi.org/10.1017/jfm.2011.154 Published online by Cambridge University Press

$\mathscr{C}_+$ on semicircles which are expanded from cone $\mathscr{C}_+$ and its translations by cutting on line $\varphi = 0$. The radial coordinate is the length from the apex of the cones and the radius of the semicircle is $\sqrt{3}$, whereas the azimuth is $\varphi/2$ ranging between 0 and π. Figure 10(e) represents the flow on cone $\mathscr{C}_+$ itself, and the others on those translated from $\mathscr{C}_+$ by p_+ normal to the surface. The values of p_+ are (a) -0.016, (b) -0.012, (c) -0.008, (d) -0.004, (e) 0, (f) 0.004, (g) 0.008 and (h) 0.012. Figure 10(a) represents the innermost cone and (h) the outermost. Segments AB (identical to AF), AC, AD and AE in (e) are the cross-sections of $\mathscr{C}_+$ with the (x, y)-plane ($y > 0$), (z, x)-plane ($z < 0$), (x, y)-plane ($y < 0$) and the (z, x)-plane ($z > 0$), respectively. The centres of segments AB and AC correspond to the origins in figures 9(a,b) and 9(c,d), respectively. The in-plane component of velocity is shown by arrows, and the normal component by grey for the direction from inside to outside of the cone and by white for *vise versa*. The dotted semicircle indicates the cross-section with cone $\mathscr{C}_-$.

We see in all the panels that the streamlines in the semicircles form rectangular hyperbola with the horizontal and vertical lines as the asymptotes (as will be derived in § 5.4.2; see (5.47) and recall $|b| \ll 1$ (4.25b)) except for the neighbourhood of the cross-section of the two cones and the pole (the origin of the semicircle, e.g. A in e). This means that the asymptotes of the streamlines are nearly either on the (x, y)-plane or on the (z, x)-plane. By surveying the size of arrows in the order from (a) to (h), we find that the in-plane component of velocity takes the maximum in magnitude at (f) and the second local maximum at (c), and that it changes the direction once at (d). This reflects that the velocity changes rapidly across the thin shear layer of thickness $O(\delta^{2/5}) = 10^{-2.4} \sim 0.0040$ and that it has two peaks of opposite senses across the layer as seen in figure 9.

The normal component takes large values near the cross-section (shown by a dotted semicircle) with cone $\mathscr{C}_-$ owing to the interference between the two conical shear layers. Let us have a closer look at the velocity field near the line $\varphi = \pi$ (segment AD in e), which corresponds to the negative y side of cross-section with the (x, y)-plane (also corresponds to the line pointing lower-left from $x = 1$ in figure 12a). The in-plane component of velocity along this line inside the cone (a–d) is pointed from the base to the apex of the cone, and *vice versa* outside of the cone (e–h). The flow in the conical shear layer $\mathscr{C}_-$ is contrary to that in $\mathscr{C}_+$; it points from the apex to the base at the inner side of the cone and *vice versa* at the outer side. As a result, as seen near the dotted circle in (a)–(d), the flow points inside (shown by white) of the cone at a larger radius, whereas it points outside (shown by grey) of the cone at a smaller radius. Another characteristic feature of the normal velocity is that it changes the sign across segments AC and AE in most of the panels, suggesting that the y-component of velocity is dominant (see figure 13).

5.3. *Flow outside conical shear layers*

In the preceding subsection, we paid our attention to the conical shear layers, the velocity in which is much stronger than elsewhere. Here instead we look at the region outside the shear layers which occupies most of the volume of the sphere. The interior of the sphere is separated into four domains by the two conical shear layers, which are indicated by A, B, C, D in figure 11. In the following, we use these symbols to identify the respective domains.

In figure 12 we plot the velocity field, calculated from (5.5a)–(5.5c), on eight meridional planes of different azimuthal angle φ including the spin (x) axis, which is horizontal in this figure. Figure 12(a) represents the (x, y)-plane, and the azimuthal

https://doi.org/10.1017/jfm.2011.154 Published online by Cambridge University Press

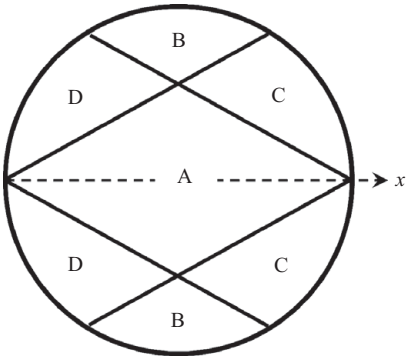


FIGURE 11. The interior of a sphere is separated into four domains by two conical shear layers.

angle φ increases by $\pi/8$ from (a) to (i). Figure 12(e) corresponds to the (x, z)-plane, and (i) is the same as (a) but seen from the opposite side. The in-plane component of velocity is represented by arrows, whereas the normal component by contours with grey and white indicating the directions either out of and into the page, respectively. The oblique straight lines, which are the contours of normal velocity at the high levels, show the cross-sections with two conical shear layers. The in-plane component of velocity in the shear layers is not plotted because extremely long arrows there would disturb the figure. We observe in the (x, y)-plane (figures 12a and i) that there are swirling motions in each of the domains separated by the conical shear layers. They all are cyclonic, i.e. rotate around the precession (z) axis in the same direction as the precession (anti-clockwise in a–d and clockwise in f–i). The in-plane component is larger and the normal component is smaller in (a) and (i), and *vice versa* in (e). This indicates the two-dimensional structure of the flow except for the close vicinity of the shear layers to which the flow is nearly tangential (figure 14). It is consistent with the cyclonic flows with axis slightly inclined to the positive y-axis that the grey for the normal components distributes in the left side of each domain.

In figure 13 we plot the velocity field on eight planes perpendicular to the spin axis. The in-plane component of velocity is drawn with arrows and the cross-sections with two cones $\mathscr{C}_{\pm}$ with dotted circles. The separated domains are B and A from outside in (a), B, C and A in (b)–(d), and C and A in (e)–(h). On $x = 0$, the velocity is perpendicular to the plane (see figure 12a) and the in-plane component is zero. The behaviour of the flow is quite different from domain to domain. The y-component is dominant as a whole, especially in domain A, which reflects that the flow is nearly two-dimensional parallel to the (x, y)-plane. Those arrows of opposite direction across the dotted circle are the manifestation that the shear layers are composed of a pair of counter flows.

In figure 14 we plot the velocity field in planes perpendicular to the precession axis which points out of the page. The in-plane component of velocity is drawn with lines, whereas the normal component with grey for the positive z-direction and with white for the negative. The cyclonic swirling flows are seen in each domain separated by the shear layers in (a). As z increases, two swirling flows belonging to the same domain merge into one. This occurs in domains C and D during $(b) \rightarrow (d)$, and in B during $(e) \rightarrow (g)$. The centre of swirling flow as well as the pattern of the normal component of velocity shifts to the positive y-direction as z increases in all the domains. In domain A the normal velocity is, as a whole, positive for $x < 0$ and negative for $x > 0$. This implies

https://doi.org/10.1017/jfm.2011.154 Published online by Cambridge University Press

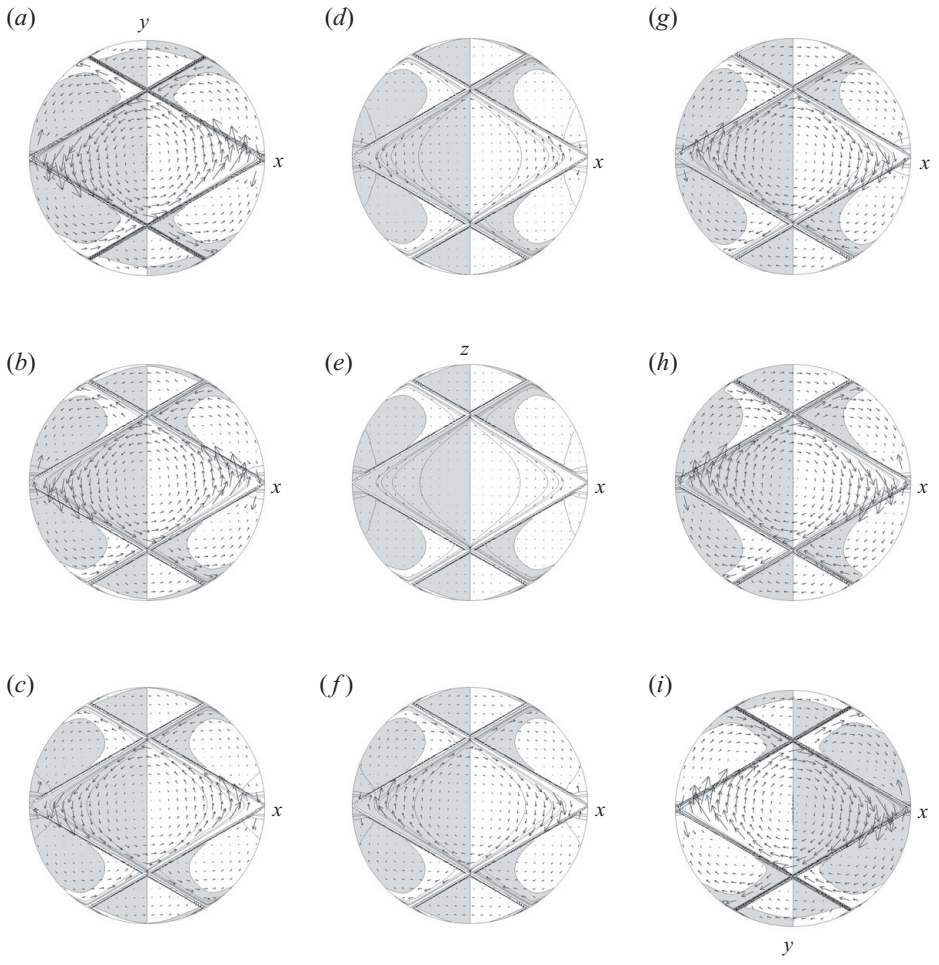


FIGURE 12. The velocity field on the meridional planes. The in-plane component of velocity is represented by arrows and the normal component by contours with grey and white indicating the directions out of or into the paper, respectively. The contour levels are $\pm 10n$, $n = 0$, 1, 2, 3, 4. (*a*) $\varphi/\pi = 0$, (*b*) 1/8, (*c*) 1/4, (*d*) 3/8, (*e*) 1/2, (*f*) 5/8, (*g*) 3/4, (*h*) 7/8, (*i*) 1. $\delta = 10^{-6}$.

that the axis of swirling flow, which is cyclonic, inclines to the positive y-direction from the z-axis. In domain B the centre of swirling flow moves along the cone.

5.4. *Detailed structure*

In the last three subsections, we described the flow in the inviscid region based on the numerical solution of (2.17). Here, we perform another asymptotic analysis to examine the detailed structure of the conical shear flow.

5.4.1. *Behaviour of the function* $F(X)$

As seen in figure 7, the solution $F(X)$ $(-1 \leqslant X \leqslant 1)$ to the integral equation (2.17) has sharp peaks at $X = \pm 1/2$ and $X = \pm 1$. Here we derive these peaks analytically.

We begin by noting that the argument $[(\cos\theta)/2 + (\sqrt{3}\sin\theta\cos\lambda)/2]$ of F in (2.17) runs between -1 and $+1$ and that the maximum and minimum are attained at $(\cos\theta, \cos\lambda) = (1/2, 1)$ and $(-1/2, -1)$, respectively. Since $B(\cos\theta)$ is an odd

https://doi.org/10.1017/jfm.2011.154 Published online by Cambridge University Press

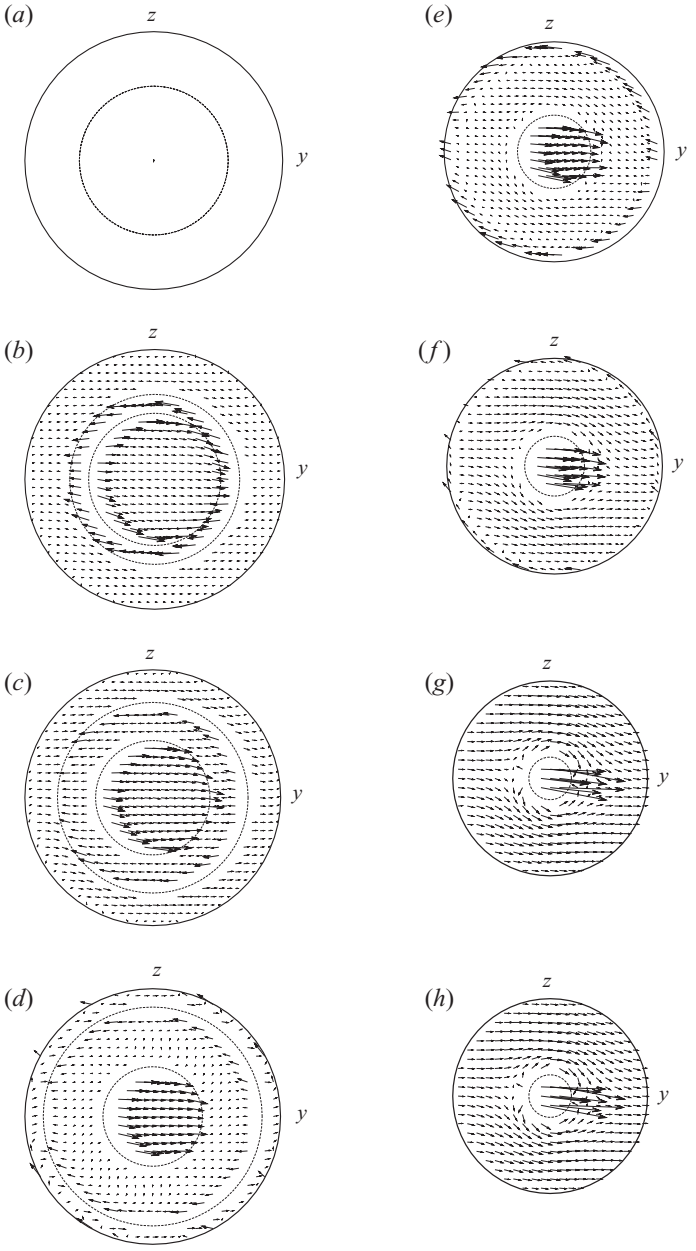


FIGURE 13. The velocity field on planes perpendicular to the spin (x) axis. The in-plane component of velocity is shown by arrows. The dotted circles indicate the cross-sections with two cones $\mathscr{C}_{\pm}$. The velocity in the shear layers is not drawn for brevity. (*a*) $x = 0$, (*b*) 0.125, (*c*) 0.25, (*d*) 0.375, (*e*) 0.5, (*f*) 0.625, (*g*) 0.75, (*h*) 0.875. $\delta = 10^{-6}$.

function of $\cos\theta$ (see (4.21)), the function $F(X)$ can also be odd, ($F(X) = -F(-X)$). Furthermore, the integration of $B(\mu)$ in a region including the critical point $\mu = \pm 1/2$ receives a negligible contribution (of higher order in δ) because the integration of the

https://doi.org/10.1017/jfm.2011.154 Published online by Cambridge University Press

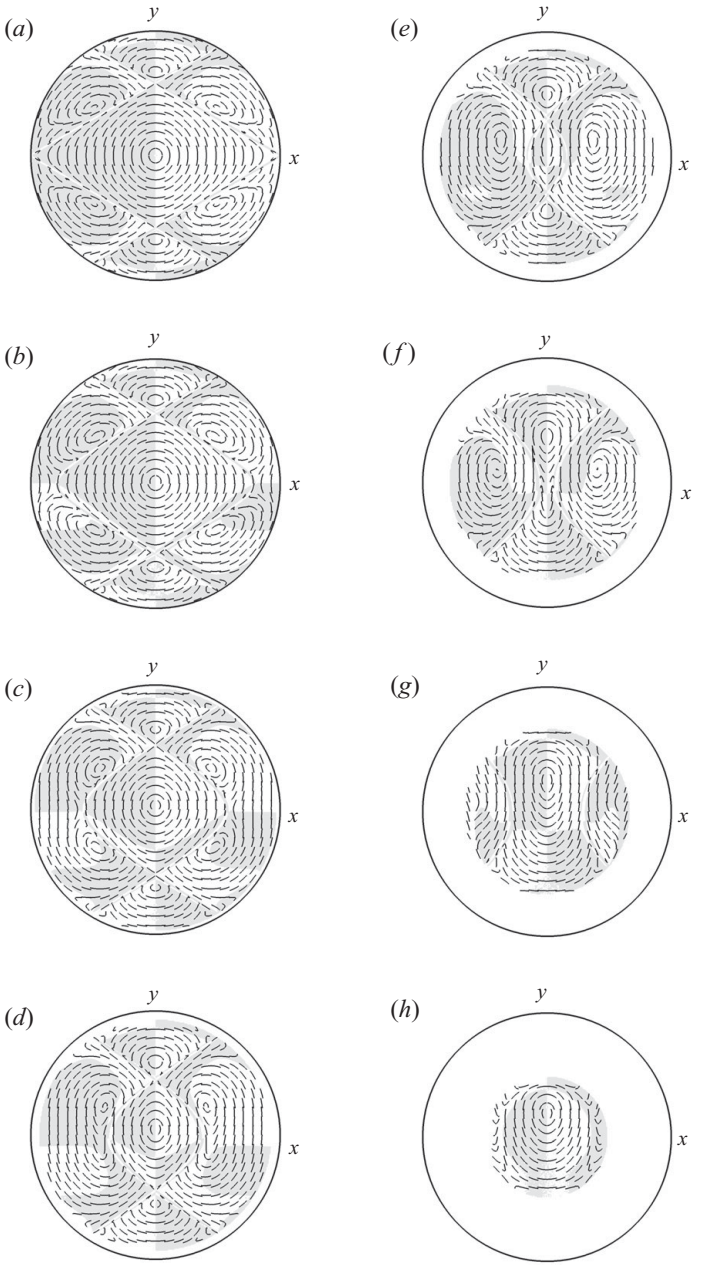


FIGURE 14. The velocity field on planes perpendicular to the precession (z) axis. The in-plane component of velocity is drawn with lines, and the direction of the normal component is shown with grey for positive z (out of the page) and with white for negative (into the page). All the swirling flow is cyclonic (anti-clockwise). (*a*) $z = 0$, (*b*) 0.125, (*c*) 0.25, (*d*) 0.375, (*e*) 0.5, (*f*) 0.625, (*g*) 0.75, (*h*) 0.875. $\delta = 10^{-6}$.

critical-region solution,

$$\int_a^b \frac{\partial Q_\infty}{\partial \eta}\, \mathrm{d}\eta = Q_\infty(b) - Q_\infty(a), \tag{5.7}$$

https://doi.org/10.1017/jfm.2011.154 Published online by Cambridge University Press

vanishes in the limit $a \to -\infty$ and $b \to \infty$ (see (4.18), figure 4, and the bottom panels in figure 6).

By keeping these facts in mind, we examine the behaviour of F under the assumption that the function $B(\mu)$ takes significant values ($O(\delta^{-3/5})$) only in the vicinity of $\mu = \pm 1/2$, i.e.

$$B(\mu) \approx \begin{cases} -\delta^{-3/5} a\, \mathrm{e}^{\mathrm{i}b} \dfrac{3\sqrt{3}\mathrm{i}}{8} \dfrac{\partial Q^*_\infty}{\partial \eta}(\eta_-) & \left(\left|\mu + \dfrac{1}{2}\right| < \mu_c\right), \\ -\delta^{-3/5} a\, \mathrm{e}^{\mathrm{i}b} \dfrac{3\sqrt{3}\mathrm{i}}{8} \dfrac{\partial Q_\infty}{\partial \eta}(\eta_+) & \left(\left|\mu - \dfrac{1}{2}\right| < \mu_c\right), \\ 0 & \text{(otherwise)}, \end{cases} \tag{5.8}$$

where $\eta_\pm = \delta^{-2/5}(\mu \mp 1/2)$ (cf. (4.21)).

We assume that the function $F(X)$ takes large values only in the vicinity of $X = \pm 1$ and $\pm 1/2$ as seen in figure 7(*a*,*b*). Note that these values of X correspond to the upper and lower limits of the argument $[(\cos\theta)/2 + (\sqrt{3}\sin\theta\cos\lambda)/2]$ of F in the integral equation (2.17) for $\mu = \pm 1/2$. In the following we consider these two neighbourhoods separately.

First, in the vicinity of $\mu = 1/2$, by putting

$$\mu = \tfrac{1}{2} + \delta^{2/5}\eta, \tag{5.9}$$

we have

$$\sin\theta = \frac{\sqrt{3}}{2}\left[1 - \frac{2}{3}\delta^{2/5}\eta - \frac{8}{9}(\delta^{2/5}\eta)^2 + O((\delta^{2/5}\eta)^3)\right]. \tag{5.10}$$

Since $(\cos\theta)/2 + (\sqrt{3}\sin\theta\cos\lambda)/2 = 1$ for $\cos\theta = 1/2$ corresponds to $\lambda = 0$, we expand $\cos\lambda$ as

$$\cos\lambda = 1 - \tfrac{1}{2}\lambda^2 + \cdots. \tag{5.11}$$

On the other hand, since $(\cos\theta)/2 + (\sqrt{3}\sin\theta\cos\lambda)/2 = -1/2$ for $\cos\theta = 1/2$ corresponds to $\lambda = \pi$, we put $\lambda = \pi + \lambda'$ and expand $\cos\lambda$ as

$$\cos\lambda = -\left(1 - \tfrac{1}{2}\lambda'^2 + \cdots\right). \tag{5.12}$$

Then, the argument of F in (2.17) is written as

$$\frac{1}{2}\cos\theta + \frac{\sqrt{3}}{2}\sin\theta\cos\lambda = \begin{cases} 1 - \dfrac{2}{3}\delta^{4/5}\eta^2 - \dfrac{3}{8}\lambda^2 + \cdots & \text{for } |\lambda| \ll 1, \\ -\dfrac{1}{2} + \delta^{2/5}\eta + \dfrac{3}{8}\lambda'^2 + \cdots & \text{for } \lambda = \pi + \lambda' \ (|\lambda'| \ll 1). \end{cases} \tag{5.13}$$

The second factor of the integrand of this equation is written as

$$\sqrt{3}\cos\theta\cos\lambda - \sin\theta\left(1 + \sin^2\lambda\right) = \begin{cases} \dfrac{4}{\sqrt{3}}\delta^{2/5}\eta - \dfrac{\sqrt{3}}{4}\lambda^2 + \cdots & \text{for } |\lambda| \ll 1, \\ -\sqrt{3} + \cdots & \text{for } \lambda = \pi + \lambda' \ (|\lambda'| \ll 1). \end{cases} \tag{5.14}$$

The leading terms in (2.17) are then expressed as

$$\int_{-c}^{c} F\left(1 - \frac{2}{3}\delta^{4/5}\eta^2 - \frac{3}{8}\lambda^2\right)\frac{4\sqrt{3}}{3}\delta^{2/5}\eta\,\mathrm{d}\lambda - \int_{-c}^{c} F\left(-\frac{1}{2} + \delta^{2/5}\eta + \frac{3}{8}\lambda'^2\right)\sqrt{3}\,\mathrm{d}\lambda' = -a\,\mathrm{e}^{\mathrm{i}b}\frac{3\sqrt{3}\mathrm{i}}{8}\delta^{-3/5}\frac{\partial Q_\infty}{\partial \eta}(\eta). \tag{5.15}$$

https://doi.org/10.1017/jfm.2011.154 Published online by Cambridge University Press

Now we assume the following scaling form of $F(X)$ near $X=\pm1$ and $X=\pm1/2$,

$$F(X)=\begin{cases}\pm\delta^{-7/5}\Phi_1\left(\sqrt{\frac{3}{2}\delta^{-4/5}(1\mp X)}\right) & \text{for } X\approx\pm1, \quad (5.16a)\\ \pm\delta^{-4/5}\Phi_2\left(\delta^{-2/5}\left(\frac{1}{2}\pm X\right)\right) & \text{for } X\approx\mp\frac{1}{2}, \quad (5.16b)\end{cases}$$

so that δ may be factored out from (5.15), and that

$$\int_{-\infty}^{\infty}\Phi_2(\eta)\,\mathrm{d}\eta=0. \tag{5.17}$$

As we shall see below (after (5.33)), the latter assumption is actually satisfied by the solution.

The above integral equation (5.15) is converted, after changing the integration variables as $\lambda=4\delta^{2/5}|\eta|s/3$ and $\lambda'=\sqrt{8/3}\delta^{1/5}s$, to

$$\mathrm{sgn}(\eta)\frac{16\sqrt{3}}{9}\eta^2\int_{-\infty}^{\infty}\Phi_1(|\eta|\sqrt{1+s^2})\,\mathrm{d}s-\sqrt{8}\int_{-\infty}^{\infty}\Phi_2(\eta+s^2)\,\mathrm{d}s=-a\,\mathrm{e}^{\mathrm{i}b}\frac{3\sqrt{3}\mathrm{i}}{8}\frac{\partial Q_\infty}{\partial\eta}(\eta). \tag{5.18}$$

Secondly, in the vicinity of $\mu=-1/2$, by putting

$$\mu=-\tfrac{1}{2}+\delta^{2/5}\eta, \tag{5.19}$$

we have

$$\sin\theta=\frac{\sqrt{3}}{2}\left[1+\frac{2}{3}\delta^{2/5}\eta-\frac{8}{9}(\delta^{2/5}\eta)^2+O((\delta^{2/5}\eta)^3)\right]. \tag{5.20}$$

Since $(\cos\theta)/2+(\sqrt{3}\sin\theta\cos\lambda)/2=1/2$ for $\cos\theta=-1/2$ corresponds to $\lambda=0$, we expand $\cos\lambda$ as

$$\cos\lambda=1-\tfrac{1}{2}\lambda^2+\cdots, \tag{5.21}$$

whereas $(\cos\theta)/2+(\sqrt{3}\sin\theta\cos\lambda)/2=-1$ for $\cos\theta=-1$ corresponds to $\lambda=\pi$, and we put $\lambda=\pi+\lambda'$ and expand

$$\cos\lambda=-\left(1-\tfrac{1}{2}\lambda'^2+\cdots\right). \tag{5.22}$$

Then the argument of F is written as

$$\frac{1}{2}\cos\theta+\frac{\sqrt{3}}{2}\sin\theta\cos\lambda=\begin{cases}\frac{1}{2}+\delta^{2/5}\eta-\frac{3}{8}\lambda^2+\cdots & \text{for } |\lambda|\ll1,\\ -1+\frac{2}{3}\delta^{4/5}\eta^2+\frac{3}{8}\lambda'^2+\cdots & \text{for } \lambda=\pi+\lambda'\ (|\lambda'|\ll1).\end{cases} \tag{5.23}$$

The second factor in the integrand of (2.17) is written as

$$\sqrt{3}\cos\theta\cos\lambda-\sin\theta(1+\sin^2\lambda)=\begin{cases}-\sqrt{3}+\cdots & \text{for } |\lambda|\ll1,\\ -\frac{4}{\sqrt{3}}\delta^{2/5}\eta+\frac{\sqrt{3}}{4}\lambda'^2+\cdots & \text{for } \lambda=\pi+\lambda'\ (|\lambda'|\ll1).\end{cases} \tag{5.24}$$

Then the leading terms in (2.17) are expressed as

$$-\int_{-c}^{c}F\left(-1+\frac{2}{3}\delta^{4/5}\eta^2+\frac{3}{8}\lambda'^2\right)\frac{4\sqrt{3}}{3}\delta^{2/5}\eta\,\mathrm{d}\lambda'$$
$$-\int_{-c}^{c}F\left(\frac{1}{2}+\delta^{2/5}\eta-\frac{3}{8}\lambda^2\right)\sqrt{3}\,\mathrm{d}\lambda'=-a\,\mathrm{e}^{\mathrm{i}b}\frac{3\sqrt{3}\mathrm{i}}{8}\delta^{-3/5}\frac{\partial Q^*_\infty}{\partial\eta}(\eta). \tag{5.25}$$

https://doi.org/10.1017/jfm.2011.154 Published online by Cambridge University Press

This integral equation is converted, after changing variables of $\lambda' = 4\delta^{2/5}|\eta|s/3$, $\lambda = \sqrt{8/3}\delta^{1/5}s$ and $\eta \to -\eta$, to

$$-\mathrm{sgn}(\eta)\frac{16\sqrt{3}}{9}\eta^2\int_{-\infty}^{\infty}\Phi_1(|\eta|\sqrt{1+s^2})\,\mathrm{d}s + \sqrt{8}\int_{-\infty}^{\infty}\Phi_2(-\eta-s^2)\,\mathrm{d}s = a\,\mathrm{e}^{\mathrm{i}b}\frac{3\sqrt{3}\mathrm{i}}{8}\frac{\partial Q_\infty}{\partial\eta}(\eta). \quad (5.26)$$

Here use has been made of the Hermitian property of $Q_\infty(\eta)$, i.e. $Q_\infty(\eta) = Q_\infty^*(-\eta)$.

Summation of (5.18) and (5.26) leads to

$$\int_{-\infty}^{\infty}(\Phi_2(\eta+s^2) - \Phi_2(-\eta-s^2))\,\mathrm{d}s = 0 \quad \text{for any } \eta. \quad (5.27)$$

This implies that $\Phi_2(\eta)$ is an even function of η, i.e.

$$\Phi_2(\eta) = \Phi_2(-\eta). \quad (5.28)$$

The even and odd parts with respect to η of (5.18) give respectively

$$\int_0^{\infty}(\Phi_2(\eta+s^2) + \Phi_2(-\eta+s^2))\,\mathrm{d}s = -a\,\mathrm{e}^{\mathrm{i}b}\frac{3\sqrt{3}}{16\sqrt{2}}\frac{\partial Q_{\infty i}}{\partial\eta}(\eta) \quad (5.29)$$

and

$$-\mathrm{sgn}(\eta)\frac{16\sqrt{3}}{9\sqrt{2}}\eta^2\int_0^{\infty}\Phi_1(|\eta|\sqrt{1+s^2})\,\mathrm{d}s + \int_0^{\infty}(\Phi_2(\eta+s^2) - \Phi_2(-\eta+s^2))\,\mathrm{d}s = a\,\mathrm{e}^{\mathrm{i}b}\frac{3\sqrt{3}\mathrm{i}}{16\sqrt{2}}\frac{\partial Q_{\infty r}}{\partial\eta}(\eta). \quad (5.30)$$

Now we introduce the Fourier transform of $\Phi_2(\eta)$ as

$$\widetilde{\Phi}_2(k) = \frac{1}{2\pi}\int_{-\infty}^{\infty}\Phi_2(\eta)\,\mathrm{e}^{-\mathrm{i}k\eta}\,\mathrm{d}\eta. \quad (5.31a)$$

The inverse transformation is

$$\Phi_2(\eta) = \int_{-\infty}^{\infty}\widetilde{\Phi}_2(k)\,\mathrm{e}^{\mathrm{i}k\eta}\,\mathrm{d}k. \quad (5.31b)$$

We see from (5.28) that the function $\widetilde{\Phi}_2(k)$ is complex and even with respect to k.

Fourier transformation of (5.29) leads to

$$\widetilde{\Phi}_2(k) = -a\,\mathrm{e}^{\mathrm{i}b}\frac{3\sqrt{3}}{16\sqrt{\pi}}\sqrt{|k|}\,\widetilde{\frac{\partial Q_{\infty i}}{\partial\eta}}(k), \quad (5.32)$$

where use has been made of $\int_0^{\infty}\cos(ks^2)\,\mathrm{d}s = \sqrt{\pi/8|k|}$ (Fresnel integral). The inverse Fourier transformation of (5.32) gives

$$\Phi_2(\eta) = -a\,\mathrm{e}^{\mathrm{i}b}\frac{3\sqrt{3}}{16\sqrt{\pi}}\,2\int_0^{\infty}\sqrt{k}\,\widetilde{\frac{\partial Q_{\infty i}}{\partial\eta}}(k)\cos(k\eta)\,\mathrm{d}k, \quad (5.33)$$

which shows that the phase of the complex function $\Phi_2(\eta)$ is constant (b (mod π)).

Since $\partial Q_{\infty i}/\partial\eta \to -|\eta|^{-3/2}/4$ ($|\eta| \to \infty$), the Fourier transform of $\partial Q_{\infty i}/\partial\eta$ behaves, around the origin, as $\widetilde{\partial Q_{\infty i}/\partial\eta} \propto \sqrt{|k|}$ ($k \to 0$). Therefore, $\widetilde{\Phi}_2(k) \propto k$ ($k \to 0$), which gives us the following two messages. One is that $\widetilde{\Phi}_2(0) = 0$, i.e. (5.31*a*) vanishes at

https://doi.org/10.1017/jfm.2011.154 Published online by Cambridge University Press

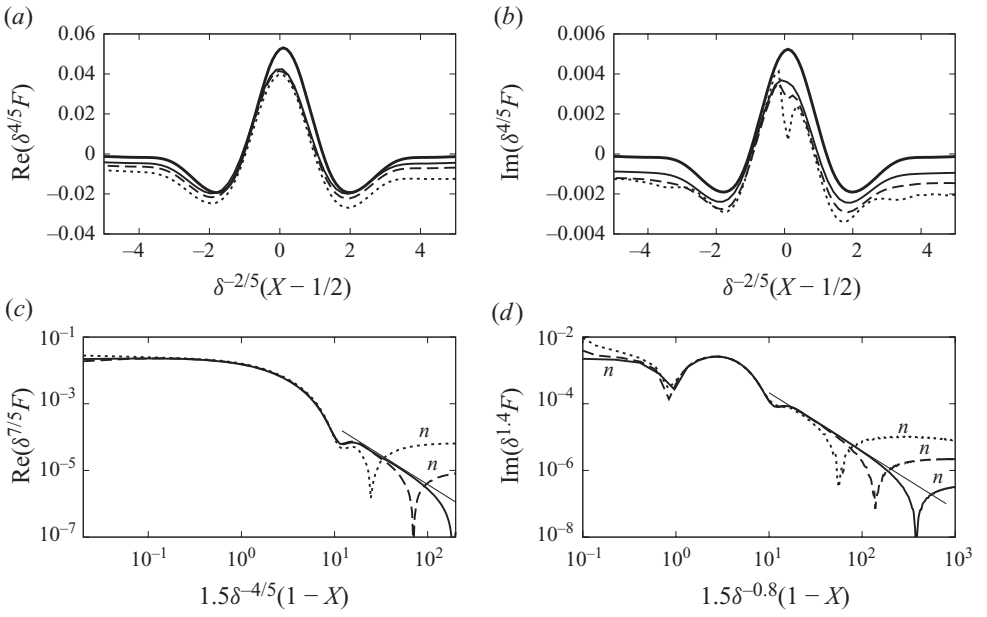


FIGURE 15. Function $F(X)$. The neighbourhoods of $X=1/2$ and $X=1$ are shown in (a,b) and (c,d), respectively, for the real part in (a,c) and the imaginary part in (b,d). The solid, dashed and dotted lines indicate the cases of $\delta=10^{-6}$, 10^{-5} and 10^{-4}, respectively. The asymptotic form (5.33) is drawn with thick lines in (a) and (b). The straight lines represent $0.006(1-X)^{-7/4}$, and the letter n indicates negative values in (c) and (d).

$k=0$, that is, the original assumption (5.17) is actually satisfied. The other is that $\Phi_2(\eta)\propto|\eta|^{-2}$ as $|\eta|\to\infty$.

The function $F(X)$ in the neighbourhood of $X=1/2$ is plotted in figures 15(a) and 15(b) for the real and imaginary parts, respectively. The abscissa and ordinate are scaled as assumed in (5.4.1b). In addition to the three lines shown in figure 7 for $\delta=10^{-4}$, 10^{-5} and 10^{-6}, the function $\Phi_2(\eta)$ calculated by (5.33) is drawn with thick lines. It is confirmed that the function $F(X)$ obeys the scaling law (5.16b) well and approaches a limiting form as $\delta\to0$.

Substitution of (5.33) into the second integral in (5.30) leads to

$$-\mathrm{sgn}(\eta)\frac{16\sqrt{3}}{9\sqrt{2}}\eta^2\int_0^\infty \Phi_1(|\eta|\sqrt{1+s^2})\,\mathrm{d}s = a\,\mathrm{e}^{\mathrm{i}b}\frac{3\sqrt{3}\mathrm{i}}{16\sqrt{2}}\left[\frac{\partial Q_{\infty r}}{\partial\eta}(\eta)+2\mathrm{i}\int_0^\infty\widetilde{\frac{\partial Q_{\infty i}}{\partial\eta}}(k)\sin(k\eta)\,\mathrm{d}k\right]. \quad (5.34)$$

The second term on the right-hand side is the Hilbert transformation of $\partial Q_{\infty i}/\partial\eta$. The right-hand side of this equation decays in proportion to $|\eta|^{-3/2}$ at large values of $|\eta|$, which leads to $\Phi_1(\eta)\propto|\eta|^{-7/2}$, and therefore (see (5.16a)),

$$F(X)\propto(1-X)^{-7/4}\quad\text{for }\delta^{4/5}\ll1-X\ll1. \quad (5.35)$$

The function $F(X)$ in the vicinity of $X=1$ is plotted, in logarithmic scales, in figures 15(c) and 15(d) for the real and imaginary parts, respectively. The parts of line attached with letter n indicate the negative value. Both axes are scaled according to (5.16a). The excellent overlapping of the three lines supports this scaling law.

https://doi.org/10.1017/jfm.2011.154 Published online by Cambridge University Press

Moreover, all of the curves touch the straight line $0.006(1-X)^{-7/4}$ shown with thin lines at large $\delta^{-4/5}(1-X)$, implying that the above asymptotic power law (5.35) actually holds.

In passing, it may be worth mentioning the effectiveness of the Legendre-polynomial expansion (see Appendix E) for solving the integral equation (2.17) numerically. As seen in figure 7, the solution has two kinds of sharp peaks at $X=\pm 1/2$ and ± 1. The latter is much higher and hard to calculate accurately. It increases very rapidly near $X=1$ as (5.35) though it may not diverge at $X=1$ but remain finite as figures 15(*c*) and 15(*d*) suggest. In fact we employed $N=2000$ as the number of truncation of the Legendre-polynomial expansion for $\delta=10^{-6}$. We obtained, for example, $F_r=5.488\cdots\times 10^6$ and $F_i=-7.041\cdots\times 10^5$ at $X=0.9999998$ which is the collocation point nearest to $X=1$. This value corresponds to the left end of the solid line in figure 15(*c*). This shows the superiority of the Legendre-polynomial expansion to express such a function of rapid variation.

5.4.2. *Structure of shear layers*

In the preceding subsection, we saw that in the limit of large Reynolds number and small Poincaré number ($Re\gg 1$, $\Gamma\ll 1$), $F(X)$ takes extremely large values in the vicinity of $X=\pm 1$ and $\pm 1/2$, and the integral of $F(X)$ over a region in which point $X=\pm 1/2$ is included vanishes (see (5.17)). Since $|x/2+(\sqrt{3}\rho\cos\lambda)/2|<1$ for $x^2+\rho^2<1$, we see in the integrals (2.16*a*)–(2.16*d*) that there is no contribution to the velocity and pressure fields in the inviscid region from $F(X)$ in the vicinity of $X=\pm 1$. Hence we examine the contribution to the integral from $F(X)$ around $X=\pm 1/2$.

For $\delta\ll 1$, $F(X)$ is approximated as

$$F(X)=\delta^{-\frac{4}{5}}\Phi_2\big(\delta^{-\frac{2}{5}}\big(X+\tfrac{1}{2}\big)\big)-\delta^{-\frac{4}{5}}\Phi_2\big(\delta^{-\frac{2}{5}}\big(X-\tfrac{1}{2}\big)\big) \tag{5.36}$$

(see (5.16*b*)). Here, the function $\Phi_2(X)$ is complex with constant argument b, is even with respect to X, decays as $|F|\propto|X|^{-2}$ as $|X|\to\infty$ and integrates out over $-\infty<X<\infty$.

Since the integrands in (5.5*a*)–(5.5*d*) have a function $F(X)$ of these properties, they take significant values only if the variation interval of the arguments, $\delta^{-2/5}(X\pm 1/2)$, of Ψ_2 is finite, that is, only when the maximum (at $\lambda=0$) or the minimum (at $\lambda=\pi$) with respect to λ ($0\leqslant\lambda<2\pi$) is, respectively, close to $1/2$ or $-1/2$ for given x and ρ. This condition is satisfied only for the coordinate (x,ρ) located near either of the following two surfaces:

$$x\pm\sqrt{3}\rho=\pm 1\quad(\mathscr{C}_{\pm}\text{, say}). \tag{5.37}$$

These are right circular cones with the spin (x) axis as the symmetry axis and with the apex angle being $\pi/3$. The apex is located at the positive (or negative) cross-point of the x-axis with the sphere for $\mathscr{C}_+$ (or $\mathscr{C}_-$).

Near the respective circular cones $\mathscr{C}_{\pm}$, the velocity and pressure fields are expressed as

$$u_x(x,\rho,\varphi)=-2^{\frac{5}{2}}\times 3^{\frac{1}{4}}\delta^{-\frac{3}{5}}q_{\pm}^{-\frac{1}{2}}W'(-p_{\pm})\cos(\varphi+b), \tag{5.38a}$$

$$u_\rho(x,\rho,\varphi)=\pm 2^{\frac{5}{2}}\times 3^{-\frac{1}{4}}\delta^{-\frac{3}{5}}q_{\pm}^{-\frac{1}{2}}W'(-p_{\pm})\cos(\varphi+b), \tag{5.38b}$$

$$u_\varphi(x,\rho,\varphi)=\mp 2^{\frac{7}{2}}\times 3^{-\frac{1}{4}}\delta^{-\frac{3}{5}}q_{\pm}^{-\frac{1}{2}}W'(-p_{\pm})\sin(\varphi+b), \tag{5.38c}$$

$$p(x,\rho,\varphi)=\pm 2^{\frac{7}{2}}\times 3^{\frac{1}{4}}\delta^{-\frac{1}{5}}q^{-\frac{3}{2}}W(-p_{\pm})\sin(\varphi+b), \tag{5.38d}$$

https://doi.org/10.1017/jfm.2011.154 Published online by Cambridge University Press

where

$$p_{\pm} = \delta^{-\frac{2}{5}} \left(\pm\frac{1}{2}x + \frac{\sqrt{3}}{2}\rho - \frac{1}{2} \right), \tag{5.39a}$$

$$q_{\pm} = \mp\frac{\sqrt{3}}{2}x + \frac{1}{2}\rho + \frac{\sqrt{3}}{2}, \tag{5.39b}$$

are respectively the coordinates normal and parallel to circular cones $\mathscr{C}_{\pm}$ in a meridional plane $\varphi = \text{const}$, the former being normalized by the shear flow thickness $\delta^{2/5}$. The function $W(\eta)$ has been introduced by

$$W(\eta) = 2\,\mathrm{e}^{-\mathrm{i}b} \int_0^{\infty} \Phi_2(\eta - s^2)\, s^2\, \mathrm{d}s, \tag{5.40a}$$

the derivative of which is written as

$$W'(\eta) = \mathrm{e}^{-\mathrm{i}b} \int_0^{\infty} \Phi_2(\eta - s^2)\, \mathrm{d}s. \tag{5.40b}$$

Note that the pressure is $O(\delta^{-1/5})$, which is smaller, by factor $\delta^{2/5}$, than the velocity $O(\delta^{-3/5})$.

The Fourier transform of (5.40*b*) gives

$$\widetilde{W}'(k) = -a\frac{3\sqrt{3}}{16\sqrt{2}} \widetilde{\frac{\partial Q_{\infty i}}{\partial \eta}}(k) \frac{1 + \mathrm{i}\ \mathrm{sgn}(k)}{2}. \tag{5.41}$$

Here, use has been made of (5.33) and

$$\int_0^{\infty} \frac{\sin kx}{x}\, \mathrm{d}x = \frac{\pi}{2}\ \mathrm{sgn}(k). \tag{5.42}$$

The inverse Fourier transform of (5.41) then yields

$$W'(\eta) = -a\frac{3\sqrt{3}}{16\sqrt{2}} \left(\frac{1}{2}\frac{\partial Q_{\infty i}}{\partial \eta}(\eta) - \int_0^{\infty} \widetilde{\frac{\partial Q_{\infty i}}{\partial \eta}}(k) \sin(k\eta)\, \mathrm{d}k \right), \tag{5.43}$$

the first term of which is even with respect to η and the second is odd. Using the numerical data of $\partial Q_{\infty i}/\partial\eta$, we can calculate $W'(\eta)$ and $W(\eta)$ by numerical integration of (5.43). In figure 16 we plot these thus obtained. The function $W(\eta)$ represents the pressure distribution across the conical shear layer, whereas the derivative $W'(\eta)$ the velocity distribution.

The normal (p) and parallel (q) components of velocity near the circular cones $\mathscr{C}_{\pm}$ are calculated, from (5.38*a*) and (5.38*b*), to be

$$u_p(x, \rho, \varphi) = 0, \tag{5.44a}$$

$$u_q(x, \rho, \varphi) = \pm 2^{\frac{7}{2}} \cdot 3^{-\frac{1}{4}} \delta^{-\frac{3}{5}} q_{\pm}^{-\frac{1}{2}} W'(-p_{\pm}) \cos(\varphi + b). \tag{5.44b}$$

From these two velocity components and the third one (5.38*c*), we see that the velocity field $O(\delta^{-3/5})$ near the conical shear layer is parallel to the layer and that the parallel component is simply written as

$$u_q(x, \rho, \varphi) = u_q(x, \rho, -b) \cos(\varphi + b), \tag{5.45a}$$

$$u_{\varphi}(x, \rho, \varphi) = -u_q(x, \rho, -b) \sin(\varphi + b), \tag{5.45b}$$

https://doi.org/10.1017/jfm.2011.154 Published online by Cambridge University Press

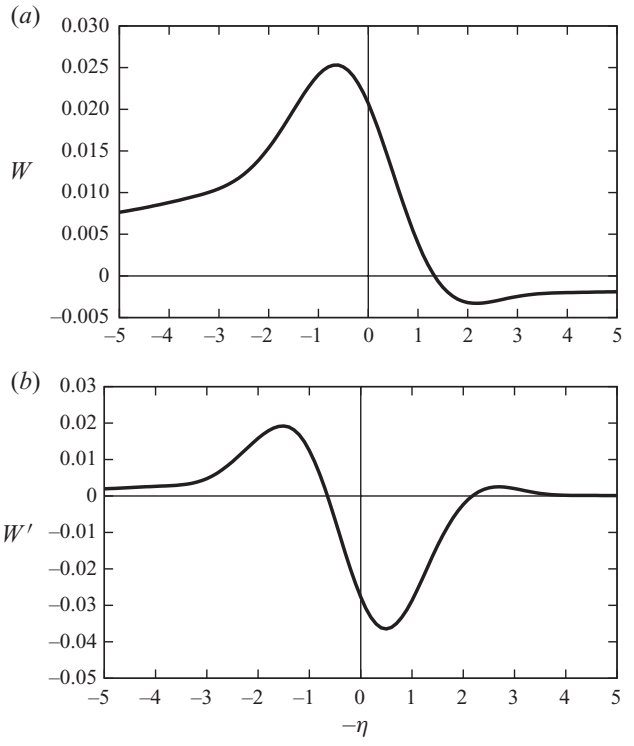


FIGURE 16. Function $W(\eta)$ and its derivative.

that is, the magnitude of the shear velocity is independent of φ and the direction (angle to the generating line of the cones $\mathscr{C}_{\pm}$) varies linearly with φ. The velocity profile in the shear layer shown in figure 9 is well expressed by (5.44*b*)–(5.45*b*).

The velocity field in surfaces parallel to the shear layer as shown in figure 10 can be expressed explicitly. We take one of the cones, $\mathscr{C}_{+}$, cut it by the line $\varphi = 0$, expand it into a semicircle of radius $\sqrt{3}$ and introduce the polar coordinate (s_{CL}, φ_{CL}) through $s_{CL} = q_{+}$ and $\varphi_{CL} = \varphi/2$. Then the radial and azimuthal components of velocity on the semicircle are written as

$$u_{s_{CL}}(s_{CL}, \varphi_{CL}) = u_{s_{CL}}\left(s_{CL}, -\tfrac{1}{2}b\right)\cos(2\varphi_{CL} + b), \tag{5.46a}$$

$$u_{\varphi_{CL}}(s_{CL}, \varphi_{CL}) = u_{s_{CL}}\left(s_{CL}, -\tfrac{1}{2}b\right)\sin(2\varphi_{CL} + b). \tag{5.46b}$$

The streamlines on this surface are obtained, by integrating $\mathrm{d}s_{CL}/u_{s_{CL}} = s_{CL}\,\mathrm{d}\varphi_{CL}/u_{\varphi_{CL}}$, as

$$s_{CL}^2 \sin(2\varphi_{CL} + b) = \text{const.} \tag{5.47}$$

This represents a group of rectangular hyperbola with two asymptotes, $\varphi_{CL} = -b/2$ and $\varphi_{CL} = -(b + \pi)/2$ as observed in figure 10. The streamline (5.47) is expressed as $\rho^2 \sin(\varphi + b) = \text{const}$ and $x + \sqrt{3}\rho = 1$ in the cylindrical polar coordinate (x, ρ, φ).

6. Concluding remarks

We have investigated the flow structure in a precessing sphere in the limit $Re \gg 1$ and $\Gamma \ll 1$. The most important finding is the solution to the critical-region equation (4.13*a*) which was derived by Roberts and Stewartson in 1963. This equation

https://doi.org/10.1017/jfm.2011.154 Published online by Cambridge University Press

had never been solved over such a long time since then, though it had been repeatedly referred to in the context of the breakdown of the boundary-layer analysis. The reason may be attributed to the lack of the boundary conditions (i.e. (4.15*a*)–(4.15*d*), (4.17*a*) and (4.17*b*)) to supplement the equation, which were obtained in § 4. Using the solution to the critical-region equation, we were able to determine the velocity field in the interior of the sphere, including the velocity profile across the conical shear layers.

The present results have the following implications. First, a precessing sphere has long attracted people's attention as a model of the outer core of the Earth with relation to the generation and sustenance mechanism of the geomagnetic field. The limit $Re \gg 1$ and $\Gamma \ll 1$ is of particular interest because the melted iron in the outer core is inferred to be in this parameter range (Roberts & Glatzmaier 2000). It is crucial for the study of dynamo action to know the flow characteristics in this limit. Apart from the geophysical application, the flow in a precessing sphere is considered as one of the canonical fluid systems. Both the geometry (a sphere) of the container and the generation mechanism (two rotations) of the flow are simple and fundamental. Because of this simplicity three different approaches (theoretical, numerical and experimental) to the study of the flow can be performed under exactly the same boundary conditions and their results can be compared with each other with high accuracy. Secondly, the flow easily exhibits a variety of states, either laminar or turbulent by changing the control parameters (Re, Γ, and the angle between the spin and precession axes). Up to now, however, the flow in a precessing sphere has not been studied systematically. But see some of our recent works (Goto *et al.* 2007; Kida & Nakayama 2007; Kida, Nakayama & Honda 2009). Even the stability boundary of the steady flow is not known in the whole parameter space, which we are currently studying by a numerical approach. So far we have found that the critical Reynolds number above which the steady flow is unstable is about $Re = 1040$ at $\Gamma = 0.181$ in the case when the two rotation axes are orthogonal. It is anticipated by our laboratory experiment that the stability boundary may have the asymptote like $\Gamma \propto Re^{-\alpha}$, $\alpha \approx 0.9$ (a paper in preparation). In order to obtain such an asymptote theoretically, the steady velocity flow obtained in the present paper may serve as the base flow for the linear stability analysis. Thirdly, the scale and structure of the conical share layers have been revealed quantitatively. The velocity is $O(\Gamma Re^{3/10})$ in the conical shear layers of width $O(Re^{-1/5})$. They carry the flux $O(\Gamma Re^{1/10})$ in total, which is larger, by a factor $O(Re^{1/10})$, than the flux from the rest of the boundary where the radial component of velocity is $O(\Gamma)$. The velocity gradient in the conical shear layers is $O(\Gamma Re^{1/2})$ which is much larger, by a factor $O(Re^{1/2})$, than in the rest of the interior. Therefore the conical shear layers should play significant dynamical roles, including mixing, energy dissipation, etc. With this relation, we have observed very recently in our laboratory experiment such an interesting flake pattern that was observed before by Vanyo *et al.* (1995) (see their figures 2*a*,*b* and 7). This pattern may be explained by the use of conical shear layers (a paper in preparation).

In the present paper, the velocity field in the inviscid region was determined at $O(\Gamma\delta^0)$ except for the solid-body-rotation flow at this order. In the same manner as the solid-body-rotation flow (characterized by a (4.25*a*) and b (4.25*b*)) of $O(\Gamma\delta^{-1})$ was determined by applying the boundary-layer solution to the condition (2.18) (described in § 3), that of $O(\Gamma\delta^0)$ will be determined by applying the boundary-layer solution at the next order $O(\Gamma\delta)$ to (2.18) with the right-hand side being zero. This analysis will be published elsewhere.

The success of the Legendre-polynomial expansion of a non-regular function defined over a finite domain is a by-product of the present work. This expansion was

https://doi.org/10.1017/jfm.2011.154 Published online by Cambridge University Press

introduced to solve the integral equation (2.17), the solution $F(X)$ of which turned out to vary very rapidly at $X=\pm 1/2$ and ± 1 (see figures 7*a* and *b*). As shown by three examples in appendix E, a finite series of the Legendre-polynomial expansion of a non-regular function reproduces the original one excellently well at the zero points of the Legendre polynomials of the order of the truncated number. Therefore this method may be superior to the so-called Padé approximation (Hesthaven, Kaber & Lurati 2006).

The author would like to express his cordial gratitude to Professors M Yamada and S. Goto for their invaluable suggestions to this study, and to Dr M. Shimizu and Messrs. N. Honda and T. Nakamura for their helpful contributions during this work. Deepest thanks are also due to one of the anonymous referees for his/her constructive comments. The numerical calculations were carried out on SX8 at YITP in Kyoto University.

Appendix A. Non-orthogonal precessing rotation

In § 2 we have shown that the velocity field $\boldsymbol{u}^{(1)}$ of first order in the Γ expansion is described by (2.8)–(2.10) when the axes of the spin and precession rotations are orthogonal to each other. Here we prove that it can be described by essentially the same equation even when the two rotation axes are oblique.

Let α $(0 \leqslant \alpha \leqslant \pi/2)$ be an angle between the two axes and denote the precession angular velocity by $\boldsymbol{\Omega}_p = \Omega_p(\widehat{\boldsymbol{x}}\cos\alpha + \widehat{\boldsymbol{z}}\sin\alpha)$. Then, $\boldsymbol{u}^{(1)}$ is governed by

$$(\boldsymbol{u}_{solid}\cdot\nabla)\boldsymbol{u}^{(1)} + (\boldsymbol{u}^{(1)}\cdot\nabla)\boldsymbol{u}_{solid} + \nabla p^{(1)} - \frac{1}{Re}\nabla^2\boldsymbol{u}^{(1)} = -2(\widehat{\boldsymbol{x}}\cos\alpha + \widehat{\boldsymbol{z}}\sin\alpha)\times\boldsymbol{u}_{solid} \quad (A\,1)$$

(in place of (2.8)) together with (2.9) and (2.10). The solid-body rotation $\boldsymbol{u}_{solid}$ is given by (2.6*a*).

We introduce new variables $\widetilde{\boldsymbol{u}}^{(1)}$ and $\widetilde{p}^{(1)}$ through

$$\boldsymbol{u}^{(1)} = \widetilde{\boldsymbol{u}}^{(1)}\sin\alpha, \quad (A\,2a)$$

$$p^{(1)} = \widetilde{p}^{(1)}\sin\alpha + (\widehat{\boldsymbol{x}}\times\boldsymbol{r})^2\cos\alpha. \quad (A\,2b)$$

Then, it is straightforward to show that

$$(\boldsymbol{u}_{solid}\cdot\nabla)\widetilde{\boldsymbol{u}}^{(1)} + (\widetilde{\boldsymbol{u}}^{(1)}\cdot\nabla)\boldsymbol{u}_{solid} + \nabla\widetilde{p}^{(1)} - \frac{1}{Re}\nabla^2\widetilde{\boldsymbol{u}}^{(1)} = -2\widehat{\boldsymbol{z}}\times\boldsymbol{u}_{solid}, \quad (A\,3)$$

$$\nabla\cdot\widetilde{\boldsymbol{u}}^{(1)} = 0 \quad (A\,4)$$

and

$$\widetilde{\boldsymbol{u}}^{(1)} = 0 \quad (\text{on } |\boldsymbol{r}| = 1). \quad (A\,5)$$

These three equations are equivalent to (2.8)–(2.10).

Appendix B. Solution to the Poincarè equation

Here we derive the general solution to the Poincarè equation,

$$\left(\frac{\partial^2}{\partial\rho^2} + \frac{1}{\rho}\frac{\partial}{\partial\rho} - \frac{1}{\rho^2} - \sigma^2\frac{\partial^2}{\partial x^2}\right)v = 0, \quad (B\,1)$$

where σ is a positive number, equal to $\sqrt{3}$ in (2.15).

https://doi.org/10.1017/jfm.2011.154 Published online by Cambridge University Press

Since this equation is homogeneous with respect to the independent variables ρ and x, the solution may be expressed by a superposition of plane waves of continuously different slopes as

$$v(x,\rho)=\int_a^b A'(\kappa)F(x+\kappa\rho)\,\mathrm{d}\kappa, \tag{B 2}$$

where $F(x)$ and $A(\kappa)$ are the twice-differentiable functions, a and b $(a>b)$ are the constants, and the prime $'$ indicates the differentiation. Substitution of (B 2) into (B 1) gives

$$\int_a^b A'(\kappa)\left((\kappa^2-\sigma^2)F''(x+\kappa\rho)+\frac{\kappa}{\rho}F'(x+\kappa\rho)-\frac{1}{\rho^2}F(x+\kappa\rho)\right)\mathrm{d}\kappa=0. \tag{B 3}$$

After integration by parts with respect to κ, this equation is reduced to

$$\begin{aligned}\left[\rho A'(\kappa)(\kappa^2-\sigma^2)F'(x+\kappa\rho)+(-(A'(\kappa)(\kappa^2-\sigma^2))'+A'(\kappa)\kappa)F(x+\kappa\rho)\right]_a^b\\ +\int_a^b\{[(A'(\kappa)(\kappa^2-\sigma^2))'-A'(\kappa)\kappa]'-A'(\kappa)\}F(x+\kappa\rho)\,\mathrm{d}\kappa=0.\end{aligned} \tag{B 4}$$

We require that this equation should be satisfied for an arbitrary function $F(x)$. The definite integral in (B 4) is identically zero if

$$[(A'(\kappa)(\kappa^2-\sigma^2))'-A'(\kappa)\kappa]'-A'(\kappa)=0, \tag{B 5}$$

which is integrated twice to give

$$(\kappa^2-\sigma^2)A'(\kappa)-\kappa A(\kappa)=-\gamma\kappa-\beta\sigma^2. \tag{B 6}$$

After one more integration, we obtain

$$A(\kappa)=\alpha\sqrt{\sigma^2-\kappa^2}+\beta\kappa+\gamma, \tag{B 7}$$

where α, β and γ are integration constants. Differentiation of (B 7) with respect to κ gives

$$A'(\kappa)=-\frac{\alpha\kappa}{\sqrt{\sigma^2-\kappa^2}}+\beta. \tag{B 8}$$

Substituting (B 8) into the first line of (B 4), we obtain

$$\rho(\alpha\kappa-\beta\sqrt{\sigma^2-\kappa^2})\sqrt{\sigma^2-\kappa^2}F'(x+\kappa\rho)-(\alpha\sqrt{\sigma^2-\kappa^2}+\beta\kappa)F(x+\kappa\rho)=0. \tag{B 9}$$

For an arbitrary $F(x)$, this equation is satisfied for two distinguished values of κ only if $\beta=0$. Then we have $\kappa=\pm\sigma$, namely $a=-\sigma$ and $b=+\sigma$, and (B 2) is reduced to

$$v(x,\rho)=\int_{-\sigma}^{\sigma}\frac{\kappa}{\sqrt{\sigma^2-\kappa^2}}F(x+\kappa\rho)\,\mathrm{d}\kappa, \tag{B 10}$$

where we put $\alpha=-1$ without loss of generality. By changing the variables $\kappa=\sigma\cos\lambda$, this equation is rewritten as

$$v(x,\rho)=\int_0^{\pi}F(x+\sigma\cos\lambda\rho)\cos\lambda\,\mathrm{d}\lambda. \tag{B 11}$$

The general solution (2.16a) in § 2 is obtained by setting $\sigma=\sqrt{3}$ and replacing $F(x)\to 2\sqrt{3}F(x/2)$ (Bondi & Lyttleton 1953).

https://doi.org/10.1017/jfm.2011.154 Published online by Cambridge University Press

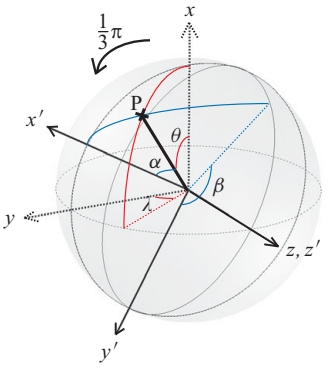


FIGURE 17. (Color online available at journals.cambridge.org/FLM) Coordinate transformation.

Appendix C. Proof of $\int_0^\pi \sin^2\theta\cos\theta$ [left-hand side of (2.17)] $\mathrm{d}\theta = 0$

The integral $\int_0^\pi \sin^2\theta\cos\theta$ [l.h.s. of (2.17)]$\mathrm{d}\theta$ is written as

$$I \equiv \int_0^\pi \mathrm{d}\theta \sin\theta \int_0^{2\pi} \mathrm{d}\lambda \times F\left(\tfrac{1}{2}\cos\theta + \tfrac{\sqrt{3}}{2}\sin\theta\cos\lambda\right)\sin\theta\cos\theta[\sqrt{3}\cos\theta\cos\lambda - \sin\theta(1+\sin^2\lambda)], \quad (C\,1)$$

which may be regarded as an integral over the whole of the unit sphere centred at the origin with the integral variables θ and λ being the polar and azimuthal angles in the Cartesian coordinate (x, y, z). Rotate this Cartesian coordinate around the z-axis by an angle $\pi/3$ and denote the resulting coordinate by (x', y', z') with the polar and azimuthal angles α and β, respectively (see figure 17) (Bondi & Lyttleton 1953).

The integral element is then transformed as

$$\sin\theta\,\mathrm{d}\theta\,\mathrm{d}\lambda = \sin\alpha\,\mathrm{d}\alpha\,\mathrm{d}\beta. \quad (C\,2a)$$

Let us denote the unit vectors in the respective coordinates in the system (x, y, z) by $\hat{\boldsymbol{x}}$, $\hat{\boldsymbol{y}}$, $\hat{\boldsymbol{z}}$, and those in (x', y', z') by $\hat{\boldsymbol{x}}'$, $\hat{\boldsymbol{y}}'$, $\hat{\boldsymbol{z}}'$. Then we have the relations $\hat{\boldsymbol{x}} = \hat{\boldsymbol{x}}'/2 - \sqrt{3}\hat{\boldsymbol{y}}'/2$, $\hat{\boldsymbol{y}} = \sqrt{3}\hat{\boldsymbol{x}}'/2 + \hat{\boldsymbol{y}}'/2$, $\hat{\boldsymbol{z}} = \hat{\boldsymbol{z}}'$, $\hat{\boldsymbol{x}}' = \hat{\boldsymbol{x}}/2 + \sqrt{3}\hat{\boldsymbol{y}}/2$, $\hat{\boldsymbol{y}}' = -\sqrt{3}\hat{\boldsymbol{x}}/2$.

A position vector $\boldsymbol{P}$ on the unit sphere centred at the origin is expressed in the two coordinate systems as

$$\boldsymbol{P} = \cos\theta\hat{\boldsymbol{x}} + \sin\theta\cos\lambda\hat{\boldsymbol{y}} + \sin\theta\sin\lambda\hat{\boldsymbol{z}}, = \cos\alpha\hat{\boldsymbol{x}}' + \sin\alpha\cos\beta\hat{\boldsymbol{y}}' + \sin\alpha\sin\beta\hat{\boldsymbol{z}}', \quad (C\,2b)$$

which gives

$$\boldsymbol{P}\cdot\hat{\boldsymbol{z}} = \sin\theta\sin\lambda = \sin\alpha\sin\beta, \quad (C\,2c)$$

$$\boldsymbol{P}\cdot\hat{\boldsymbol{x}} = \cos\theta = \frac{1}{2}\cos\alpha - \frac{\sqrt{3}}{2}\sin\alpha\cos\beta, \quad (C\,2d)$$

$$\boldsymbol{P}\cdot\hat{\boldsymbol{x}}' = \cos\alpha = \frac{1}{2}\cos\theta + \frac{\sqrt{3}}{2}\sin\theta\cos\lambda. \quad (C\,2e)$$

The last two equations lead, after elimination of $\cos\theta$, to

$$\sin\theta\cos\lambda = \frac{\sqrt{3}}{2}\cos\alpha + \frac{1}{2}\sin\alpha\cos\beta. \quad (C\,2f)$$

https://doi.org/10.1017/jfm.2011.154 Published online by Cambridge University Press

Inserting (C 2*a*)–(C 2*f*) into (C 1), we obtain the required result:

$$
\begin{aligned}
I &= \int_0^{\pi} \mathrm{d}\alpha \sin\alpha F(\cos\alpha) \int_0^{2\pi} \mathrm{d}\beta \left(\frac{1}{2}\cos\alpha - \frac{\sqrt{3}}{2}\sin\alpha\cos\beta\right) \\
&\quad \times \left[\sqrt{3}\left(\frac{1}{2}\cos\alpha - \frac{\sqrt{3}}{2}\sin\alpha\cos\beta\right)\left(\frac{\sqrt{3}}{2}\cos\alpha + \frac{1}{2}\sin\alpha\cos\beta\right)\right. \\
&\quad \left. -1 + \left(\frac{1}{2}\cos\alpha - \frac{\sqrt{3}}{2}\sin\alpha\cos\beta\right)^2 - \sin^2\alpha\sin^2\beta\right] \\
&= \int_0^{\pi} \mathrm{d}\alpha \sin\alpha F(\cos\alpha) \int_0^{2\pi} \mathrm{d}\beta \left(\frac{1}{2}\cos\alpha - \frac{\sqrt{3}}{2}\sin\alpha\cos\beta\right) \\
&\quad \times \left[-\frac{3}{2}\sin^2\alpha - \sqrt{3}\sin\alpha\cos\alpha\cos\beta + \frac{1}{2}\sin^2\alpha\cos 2\beta\right)\Big] \\
&= 0, \qquad \text{(C 3)}
\end{aligned}
$$

since the integral with respect to β vanishes.

Appendix D. Derivation of (5.2*a*) and (5.2*b*)

In order to derive (5.2*a*) and (5.2*b*), we multiply (2.17) by $\sin^2\theta P_{2n+1}(\cos\theta)$ and integrate it with respect to θ over $[0, \pi]$.

The first term on the right-hand side is (5.3) itself. The second term is explicitly calculated as

$$
\int_0^{\pi} 2\cos\theta\sin^3\theta P_{2n+1}(\cos\theta)\,\mathrm{d}\theta = \begin{cases} \dfrac{8}{15} & (n=0), \\ -\dfrac{8}{35} & (n=1), \\ 0 & (\text{otherwise}). \end{cases} \qquad \text{(D 1)}
$$

We put the integral of the left-hand side as

$$
\begin{aligned}
I_n \equiv \int_0^{\pi} \mathrm{d}\theta \sin^2\theta P_{2n+1}(\cos\theta) \int_0^{2\pi} \mathrm{d}\lambda F\left(\frac{1}{2}\cos\theta + \frac{\sqrt{3}}{2}\sin\theta\cos\lambda\right) \\
\times [\sqrt{3}\cos\theta\cos\lambda - \sin\theta(1+\sin^2\lambda)]. \qquad \text{(D 2)}
\end{aligned}
$$

By changing the integration variables from (θ, λ) to (α, β) (see Appendix C), we can rewrite (D 2) as

$$
\begin{aligned}
I_n &= \int_0^{\pi} \mathrm{d}\alpha \sin\alpha F(\cos\alpha) \int_0^{2\pi} \mathrm{d}\beta \left[P_{2n+1}\left(\frac{1}{2}\right) P_{2n+1}(\cos\alpha)\right. \\
&\quad \left. + 2\sum_{m=1}^{2n+1}(-1)^m P_{2n+1}^m\left(\frac{1}{2}\right)\frac{\Gamma(2n-m+2)}{\Gamma(2n+m+2)} P_{2n+1}^m(\cos\alpha)\cos m\beta\right] \\
&\quad \times \left[-\frac{3}{2}\sin^2\alpha - \sqrt{3}\sin\alpha\cos\alpha\cos\beta + \frac{1}{2}\sin^2\alpha\cos 2\beta\right)\Big], \qquad \text{(D 3)}
\end{aligned}
$$

https://doi.org/10.1017/jfm.2011.154 Published online by Cambridge University Press

where use has been made of the addition formula of the Legendre polynomials,

$$P_{2n+1}\left(\frac{1}{2}\cos\alpha-\frac{\sqrt{3}}{2}\sin\alpha\cos\beta\right)=P_{2n+1}\left(\frac{1}{2}\right)P_{2n+1}(\cos\alpha)$$
$$+2\sum_{m=1}^{2n+1}(-1)^m P_{2n+1}^m\left(\frac{1}{2}\right)\frac{\Gamma(2n-m+2)}{\Gamma(2n+m+2)}P_{2n+1}^m(\cos\alpha)\cos m\beta$$
$$\times\left(0\leqslant\alpha,\beta\leqslant\frac{1}{2}\pi\right). \tag{D 4}$$

Integration of (D 3) with respect to α and β gives the left-hand sides of (5.2*a*) and (5.2*b*) with the coefficient matrix $M_{n,m}$ expressed by (5.4*a*)–(5.4*c*). Note that $M_{1,0}=0$ and $I_0=0$.

Appendix E. Legendre-polynomial expansion

It is generally believed that the Taylor series of a non-regular function is divergent and that its finite series may not be a good approximant of the function. A Padé approximation, which has been developed to rescue this difficulty, does not seem to be so successful since the appearance of new singularities on the real axis may not be avoidable (Hesthaven *et al.* 2006). Here we show that a non-regular function, having a discontinuous or divergent point, can be quite accurately expressed by a finite series of Legendre-polynomial expansion if the collocation points are chosen as the zero points of the Legendre polynomial of the truncated order.

Consider a function $f(x)$ which is defined in the finite domain $-1\leqslant x\leqslant 1$ and expressed by an infinite series of Legendre polynomials $P_n(x)$ $(n=0,1,2,\ldots)$ as

$$f(x)=\sum_{n=0}^{\infty}\widetilde{f}_n P_n(x)\quad(-1\leqslant x\leqslant 1), \tag{E 1}$$

where the expansion coefficient $\widetilde{f}_n$ is given by an integral,

$$\int_{-1}^{1}f(x)P_n(x)\,\mathrm{d}x=\frac{2}{2n+1}\widetilde{f}_n\quad(n=0,1,\ldots). \tag{E 2}$$

We approximate this integral by the N-point Gaussian quadrature and consider a set of simultaneous linear equations for N unknowns f_i $(i=0,1,\ldots,N-1)$,

$$\sum_{i=0}^{N-1}w_i P_n(x_i)f_i=\frac{2}{2n+1}\widetilde{f}_n\quad(n=0,1,\ldots,N-1), \tag{E 3}$$

where x_i $(i=0,1,\ldots,N-1;\ -1<x_0<x_1<\cdots<x_{N-1}<1)$ are the zero points of $P_N(x)$ and

$$w_i=\frac{2}{\left(1-x_i^2\right)P_N'(x_i)^2}\quad(i=0,1,\ldots,N-1) \tag{E 4}$$

is the weight function. We propose that the solution $\{f_i\}$ of (E 3) is the approximant of $f(x_i)$. In this way we reconstruct the function $f(x)$ at the N zero points of $P_N(x)$ using the first N coefficients of the Legendre-polynomial expansion (E 1).

In order to show the usefulness of a finite series of the Legendre-polynomial expansion, we take three examples for which the exact values of expansion coefficients

https://doi.org/10.1017/jfm.2011.154 Published online by Cambridge University Press

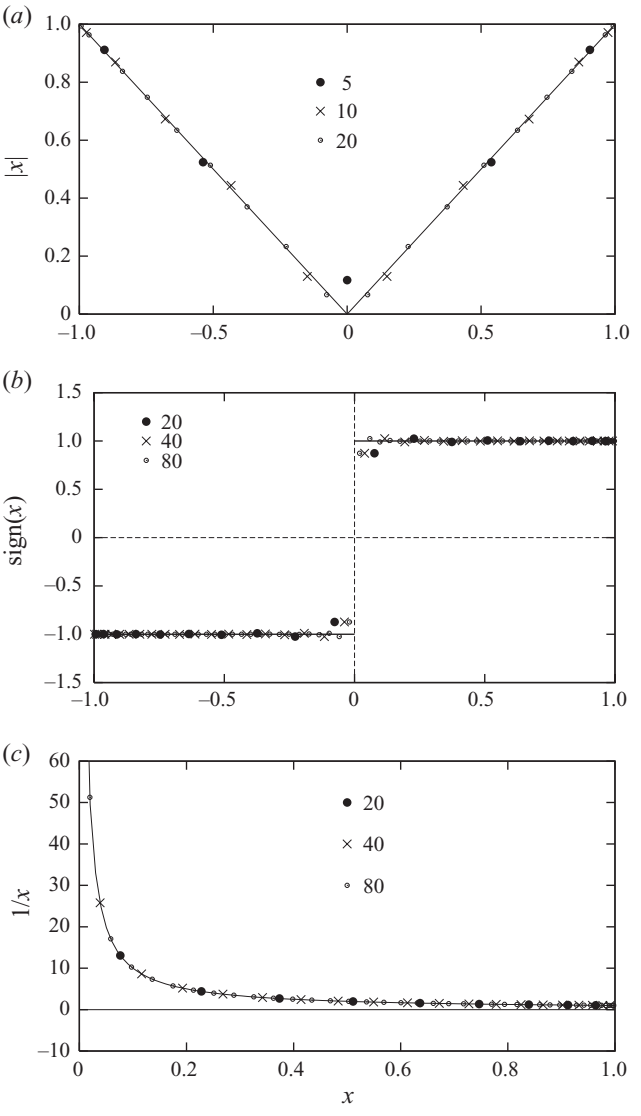


FIGURE 18. Finite series of Legendre-polynomial expansions for (*a*) $|x|$, (*b*) sign(x) and (*c*) $1/x$.

are known: they have a singular point, which is
(i) continuous but non-differentiable, e.g.

$$|x| = \frac{1}{2}P_0(x) + \sum_{n=1}^{\infty}(-1)^{n-1}\frac{(2n-3)!!}{(2n+2)!!}(4n+1)P_{2n}(x), \tag{E 5}$$

(ii) discontinuous, e.g.

$$\mathrm{sign}(x) = \sum_{n=0}^{\infty}(-1)^{n}\frac{4n+3}{2n+2}\frac{(2n-1)!!}{(2n)!!}P_{2n+1}(x), \tag{E 6}$$

https://doi.org/10.1017/jfm.2011.154 Published online by Cambridge University Press

and (iii) divergent, e.g.

$$\frac{1}{x} = \sum_{n=0}^{\infty} (-1)^n \frac{(2n)!!}{(2n+1)!!}(4n+3)P_{2n+1}(x). \tag{E 7}$$

Here, the notation !! stands for the double factorial, i.e. $m!! = m(m-2)(m-4)\cdots$ on down to either 2 or 1 depending on whether an integer m ($\geqslant 1$) is even or odd, respectively together with convention $0!! = (-1)!! = 1$.

In figure 18 we show the results of a finite Legendre-polynomial expansion of these functions. The target function is drawn with solid lines and the finite series by symbols with attached numbers of truncated orders. For all of these three cases, we find that the target functions are well reproduced by the finite series except for the closest points to the singularity. Here we have employed the zero points of the Legendre polynomials of the truncated order, which seem to be best for the collocation points. The finite series do not give a good result at other points because of the Gibbs phenomenon.

REFERENCES

Bondi, H. & Lyttleton, R. A. 1953 On the dynamical theory of the rotation of the Earth. II. The effect of precession on the motion of the liquid core. *Proc. Camb. Phil. Soc.* **49**, 498–515.

Busse, F. H. 1968 Steady fluid flow in a precessing spheroidal shell. *J. Fluid Mech.* **33**, 739–751.

Goto, S., Ishii, N., Kida, S. & Nishioka, M. 2007 Turbulence generator using a precessing sphere. *Phys. Fluids* **19**, 061705.

Greenspan, H. P. 1968 *The Theory of Rotating Fluids*. Cambridge University Press.

Hesthaven, J. S., Kaber, S. M. & Lurati, L. 2006 Padé-Legendre interpolants for Gibbs reconstruction. *J. Sci. Comput.* **28**, 337–359.

Hollerbach, R. & Kerswell, R. R. 1995 Oscillatory internal shear layers in rotating and precessing flows. *J. Fluid Mech.* **298**, 327–339.

Kerswell, R. R. 1995 On the internal shear layers spawned by the critical regions in oscillatory Ekman boundary Layers. *J. Fluid Mech.* **298**, 311–325.

Kida, S. & Nakayama, K. 2008 Helical flow structure in a precessing sphere. *J. Phys. Soc. Japan* **77** 054401.

Kida, S., Nakayama, K. & Honda, N. 2009 Streamline tori in a precessing sphere at small Reynolds numbers. *Fluid Dyn. Res.* **41**, 011401.

Malkus, W. V. R. 1968 Precession of the earth as the cause of geomagnetism. *Science* **160**, 259–264.

Noir, J., Brito, D., Aldridge, K. & Cardin, P. 2001*a* Experimental evidence of inertial waves in a precessing spheroidal cavity. *Geophy. Res. Lett.* **28**, 3785–3788.

Noir, J., Jault, D. & Cardin, P. 2001*b* Numerical study of the motions within a slowly precessing sphere at low Eckman number. *J. Fluid Mech.* **437**, 282–299.

Roberts, P. H. & Glatzmaier, G. A. 2000 Geodynamo theory and simulations. *Rev. Mod. Phys.* **72**, 1081–1123.

Roberts, P. H. & Stewartson, K. 1963 On the stability of a Maclaurin spheroid of small viscosity. *Astrophys. J.* **137**, 777–790.

Tilgner, A. & Busse, F. H. 2001 Fluid flows in precessing spherical shells. *J. Fluid Mech.* **426**, 387–396.

Vanyo, J., Wilde, P., Cardin, P. & Olson, P. 1995 Experiments on precessing flows in the Earth's liquid core. *Geophys. J. Intl* **121**, 136–142.

https://doi.org/10.1017/jfm.2011.154 Published online by Cambridge University Press